

Finding the chiral gravitational wave background of an axion- $SU(2)$ inflationary model using CMB observations and laser interferometers

Ben Thorne,^{1,2} Tomohiro Fujita,^{3,4} Masashi Hazumi,^{1,5,6,7} Nobuhiko Katayama,¹
Eiichiro Komatsu,^{1,8} and Maresuke Shiraishi^{1,9}

¹*Kavli Institute for the Physics and Mathematics of the Universe (Kavli IPMU, WPI), UTIAS,
The University of Tokyo, Chiba 277-8583, Japan*

²*Oxford Astrophysics, Denys Wilkinson Building, Keble Road, Oxford OX1 3RH, United Kingdom*

³*Stanford Institute for Theoretical Physics and Department of Physics, Stanford University,
Stanford, California 94306, USA*

⁴*Department of Physics, Kyoto University, Kyoto 606-8502, Japan*

⁵*Institute of Particle and Nuclear Studies, KEK, 1-1 Oho, Tsukuba, Ibaraki 305-0801, Japan*

⁶*SOKENDAI (The Graduate University for Advanced Studies), Hayama, Miura District,
Kanagawa 240-0115, Japan*

⁷*Institute of Space and Astronautical Studies (ISAS), Japan Aerospace Exploration Agency (JAXA),
Sagamihara, Kanagawa 252-5210, Japan*

⁸*Max Planck Institute for Astrophysics, Karl-Schwarzschild-Straße 1, 85748 Garching, Germany*

⁹*Department of General Education, National Institute of Technology, Kagawa College, 355 Chokushi-cho,
Takamatsu, Kagawa 761-8058, Japan*



(Received 12 July 2017; published 9 February 2018)

A detection of B-mode polarization of the cosmic microwave background (CMB) anisotropies would confirm the presence of a primordial gravitational wave background (GWB). In the inflation paradigm, this would be an unprecedented probe of the energy scale of inflation as it is directly proportional to the power spectrum of the GWB. However, similar tensor perturbations can be produced by the matter fields present during inflation, breaking the simple relationship between energy scale and the tensor-to-scalar ratio r . It is therefore important to find ways of distinguishing between the generation mechanisms of the GWB. Without doing a full model selection, we analyze the detectability of a new axion- $SU(2)$ gauge field model by calculating the signal-to-noise ratio of future CMB and interferometer observations sensitive to the chirality of the tensor spectrum. We forecast the detectability of the resulting CMB temperature and B-mode (TB) or E-mode and B-mode (EB) cross-correlation by the LiteBIRD satellite, considering the effects of residual foregrounds, gravitational lensing, and assess the ability of such an experiment to jointly detect primordial TB and EB spectra and self-calibrate its polarimeter. We find that LiteBIRD will be able to detect the chiral signal for $r_* > 0.03$, with r_* denoting the tensor-to-scalar ratio at the peak scale, and that the maximum signal-to-noise ratio for $r_* < 0.07$ is ~ 2 . We go on to consider an advanced stage of a LISA-like mission, which is designed to be sensitive to the intensity and polarization of the GWB. We find that such experiments would complement CMB observations as they would be able to detect the chirality of the GWB with high significance on scales inaccessible to the CMB. We conclude that CMB two-point statistics are limited in their ability to distinguish this model from a conventional vacuum fluctuation model of GWB generation, due to the fundamental limits on their sensitivity to parity violation. In order to test the predictions of such a model as compared to vacuum fluctuations, it will be necessary to test deviations from the self-consistency relation or use higher order statistics to leverage the non-Gaussianity of the model. On the other hand, in the case of a spectrum peaked at very small scales inaccessible to the CMB, a highly significant detection could be made using space-based laser interferometers.

DOI: [10.1103/PhysRevD.97.043506](https://doi.org/10.1103/PhysRevD.97.043506)

I. INTRODUCTION

Over the past two decades, the temperature and polarization anisotropies of the cosmic microwave background (CMB) have been measured with increasing sensitivity,

ushering in the era of “precision cosmology”. It is the aim of the next generation of CMB experiments to better measure the polarization of the CMB in order to detect its primordial B-mode polarization, parametrized by r , the ratio between tensor and scalar perturbations, which would

provide strong evidence for the presence of a primordial gravitational wave background (GWB) (see, e.g., [1–3] for review). Normally, the GWB is produced only by quantum fluctuations of the vacuum during inflation and is consequently simply related to the energy density of inflation: $\rho_{\text{inf}}^{1/4} \sim (\frac{r}{0.01})^{1/4} 1.04 \times 10^{16}$ GeV. A measurement of the power spectrum of tensor perturbations to the metric would therefore be an extremely powerful probe of physics at GUT scales of $\sim 10^{16}$ GeV.

Given the importance of this measurement, many experiments are currently making observations of the polarized CMB, such as POLARBEAR [4], SPTPol [5], ACTPol [6], BICEP2/Keck Array [7], and Planck [8]. The best current observational constraints come from a combination of BICEP2/Keck and Planck (BKP) data to give $r < 0.07$ (95% C.L.) [7], but the next round of CMB experiments, such as the LiteBIRD satellite [9], the CORE satellite [10], and the ground-based Stage-4 [11] effort, seek to push constraints on r to $\sim 10^{-3}$. Interestingly, this search for B-modes may also be sensitive to the dynamics of subdominant fields other than the inflaton, considering the possibility of alternative gravitational wave generation scenarios. Some particular matter fields present during inflation can produce primordial tensor perturbations similar to those sourced by vacuum fluctuations. Therefore, in the event of a detection of r , we must first understand its source.

Recent efforts to provide alternative models for the generation of gravitational waves, which are also consistent with existing observations, have introduced the coupled system of the axion and gauge fields as the spectator sector in addition to the inflaton sector [12–17]. Such a setup is quite natural from the point of view of particle physics, since many high-energy theories contain axion fields and its coupling to some gauge fields, namely, the Chern-Simons term: $(\chi/f)F^{\mu\nu}\tilde{F}_{\mu\nu}$. In particular, string theory typically predicts the existence of numerous axion fields. From the view point of low-energy effective field theory, at the same time, such a dimension five interaction term is expected to exist because it respects the shift symmetry of the axion field, $\chi \rightarrow \chi + \text{constant}$. Therefore, there is strong motivation to investigate the observational consequence of their dynamics during inflation in light of the role of inflation as a unique probe of high-energy physics.

Interestingly enough, the GWB produced by the additional axion-gauge sector has several characteristic features, including non-Gaussianity, scale dependence, and chirality. A model involving a U(1) gauge field was studied first, and it was confirmed that the resulting GWB is amplified to the same level as the scalar perturbation [12,18] and hence visible in CMB B-mode observations [19] and interferometer experiments [20]. Recently, a more intriguing model due to a $SU(2)$ gauge field was also examined, achieving a surpassing GWB production against the scalar sector [13]. This yields more rich phenomenology and thus motivates us toward the assessment of its detectability.

Gravitational waves may be decomposed into modes with left (L) and right (R) handed polarization. A GWB produced by conventional vacuum fluctuations would have equal amplitudes of L and R, but the effect of the Chern-Simons term in the theory is to allow their amplitudes to differ [12,13,21]. Such a chiral GWB would have signatures observable both in CMB polarization and by laser interferometers. CMB polarization may be decomposed into modes of opposing parity: E and B [22,23]. A detection of a correlation between E- and B-modes (EB) or between temperature and B-modes (TB) would therefore be strong evidence of a parity-violating GWB [19,21,24–26]. To date, observational constraints using the CMB are consistent with no parity violation and are dominated by systematic uncertainty [26–29]. An alternative to using the CMB is to directly probe the circular polarization Stokes parameter $V(f)$, using gravitational interferometers. Interferometers are sensitive to the strain induced in their arms by passing gravitational waves and for certain detector geometries are sensitive to the polarization of the passing wave [30–33].

In this paper, we seek to provide a realistic forecast of the ability of LiteBIRD to distinguish this $SU(2)$ model proposed in Ref. [13] from the conventional GWB generation by vacuum fluctuations. LiteBIRD is a proposed CMB satellite mission with the primary science goal of detecting the GWB with $r < 10^{-3}$ [9,34,35]. Therefore, its sensitivity will be focused in the lowest 200 multipoles where the B-mode signal is both strong and relatively uncontaminated by gravitational lensing. We exclude Stage 4 from the analysis as we found that the chirality signal is contained in the multipole range $2 \lesssim \ell \lesssim 30$. Since Stage 4 experiments will have B-mode surveys over the range $\ell \gtrsim 30$ [11], they will be ill-suited to constrain chirality, and we do not consider them further. Reference [36] considers a simple model for detecting primordial chirality using the CMB and concludes that ground-based small-scale experiments are not well-suited for pursuing this signal. We also considered a CORe-type experiment, the results of which we do not include in our analysis, as they are similar to LiteBIRD due to the dominant impact of large-scale foreground residuals for both instruments. In our analysis, we include four contributions to the uncertainty in a measurement of the chiral GWB: instrumental noise, foreground residuals from the imperfect cleaning of multichannel data, gravitational lensing, and the joint self-calibration of the instrument’s polarimeter. This provides a robust assessment of LiteBIRD’s capability to detect primordial chirality.

On the other hand, laser interferometer gravitational wave observatories are sensitive to the GWB and provide probes of much smaller scales: $k_{\text{CMB}} \sim 10^{-4} \text{ Mpc}^{-1}$ vs. $k_{\text{interf}} \sim 10^{13} \text{ Mpc}^{-1}$ [20].

In the case of single-field slow-roll inflation, the tensor spectrum is expected to have a small red tilt ($n_T = -r/8$,

where n_T is the tilt of the tensor spectrum $P_h \sim k^{n_T}$, in which case modern interferometers would not be sensitive enough to make a detection. However, given the scale dependence of the model of Ref. [13] for part of the parameter space, the small-scale tensor spectrum is comparatively large. For symmetry reasons, the nominal designs of space-based gravitational interferometers are insensitive to the circular polarization of gravitational waves. Since we are interested in constraining chirality, we therefore consider “advanced” stages of the nominal design of LISA [37,38], following the proposed designs of Ref. [33], which provide equal sensitivity to both intensity and polarization of the GWB. In this paper, we show that interferometers and CMB observations provide complementary probes at different scales of the axion- $SU(2)$ ’s primordial tensor spectrum. We then consider the sensitivities of two designs of an advanced stage LISA mission and compare to constraints achieved using the CMB.

In Sec. II, we review the model proposed by Ref. [13] and its prediction for the GWB. In Sec. III, we forecast the ability of a LiteBIRD-like CMB satellite mission to detect the TB and EB correlations expected due to the chiral tensor spectrum, in the presence of foreground contamination, gravitational lensing, instrument noise, and simultaneous self-calibration of the telescope’s polarimeter. In Sec. IV, we analyze the sensitivity of space-based gravitational interferometers to the chiral gravitational background expected by this model. Finally, in Sec. V, we summarize our findings and discuss our conclusions.

II. THEORY

In this section, we will briefly review the axion- $SU(2)$ model proposed in Ref. [13]. The model is described by the following Lagrangian:

$$\mathcal{L} = \mathcal{L}_{\text{inflaton}} + \frac{1}{2}(\partial_\mu \chi)^2 - \mu^4 \left[1 + \cos\left(\frac{\chi}{f}\right) \right] - \frac{1}{4}F_{\mu\nu}^a F^{a\mu\nu} + \frac{\lambda}{4f}\chi F_{\mu\nu} \tilde{F}^{a\mu\nu}, \quad (1)$$

where $\mathcal{L}_{\text{inflaton}}$ denotes the unspecified inflaton sector which realizes inflation and the generation of the curvature perturbation compatible with the CMB observation, χ is a pseudoscalar field (axion) with a cosine-type potential, μ and f are dimensionful parameters, and λ is a dimensionless coupling constant between the axion and the gauge field. $F_{\mu\nu}^a \equiv \partial_\mu A_\nu^a - \partial_\nu A_\mu^a - g\epsilon^{abc}A_\mu^b A_\nu^c$ is the field strength of $SU(2)$ gauge field, and $\tilde{F}^{a\mu\nu} \equiv \epsilon^{\mu\nu\rho\sigma}F_{\rho\sigma}^a/(2\sqrt{-g})$ is its dual. Here, g is the self-coupling constant of the gauge field, and ϵ^{abc} and $\epsilon^{\mu\nu\rho\sigma}$ are the completely asymmetric tensors, $\epsilon^{123} = \epsilon^{0123} = 1$.

In the axion- $SU(2)$ model in the FLRW universe $g_{\mu\nu} = \text{diag}(1, -a^2(t), -a^2(t), -a^2(t))$, the $SU(2)$ gauge fields naturally take an isotropic background configuration,

$A_0^a = 0, A_i^a = a(t)Q(t)\delta_i^a$ by virtue of the coupling to the axion χ , and the transverse and traceless part of its perturbation, $t_{ij} = \delta A_j^i$ (not to be confused with the time variable, t), sources gravitational waves at the linear order. Interestingly, either of the two circular polarization modes of t_{ij} , namely, t_R or t_L , undergoes a transient instability around the horizon crossing and gets substantially amplified. Subsequently, only the corresponding polarization mode of the gravitational wave, h_R or h_L , is significantly sourced by t_{ij} , and fully chiral gravitational waves are generated. Note that the parity ($R \leftrightarrow L$) symmetry is spontaneously broken by the background evolution of the axion (i.e., the sign of $\partial_\mu \chi(t)$). In this paper, we assume the left hand modes are produced for definiteness. In Appendix A, we derive the following expression for the sourced GW power spectrum:

$$\mathcal{P}_h^{\text{L,Sourced}}(k) = r_* \mathcal{P}_\zeta \exp \left[-\frac{1}{2\sigma^2} \ln^2 \left(\frac{k}{k_p} \right) \right] \\ \mathcal{P}_h^{\text{R,Sourced}}(k) \simeq 0, \quad (2)$$

where the amplitude is parameterized by the tensor-to-scalar ratio r_* at the peak scale $k = k_p$, σ is the width of the Gaussian-shaped spectrum, and \mathcal{P}_ζ is the power spectrum of curvature perturbations. We treat r_* and σ as free parameters in our analysis, while they can be rewritten in terms of more fundamental parameters m_* , ϵ_{B*} and ΔN , as discussed in Appendix A. Note that there is no theoretical bound on r_* , while the possible values of σ are restricted by k_p as Eq. (A11). Figure 1 gives an example of how the amplitude r_* is degenerate in m_* and ϵ_{B*} , and we show an example plot of $\mathcal{P}_h^{\text{Sourced}}(k)$ for three sets of these parameters in Fig. 2.

Here, we define the power spectrum of primordial tensor perturbations to be

$$\langle h_{\mathbf{k}}^A h_{\mathbf{k}'}^{A'} \rangle = (2\pi)^3 \frac{2\pi^2}{k^3} \mathcal{P}_h^A(k) \delta^{(3)}(\mathbf{k} + \mathbf{k}') \delta_{AA'}, \quad (3)$$

where A refers to the circular polarization of the gravitational wave with the momentum vector \mathbf{k} : $A = L, R$. For

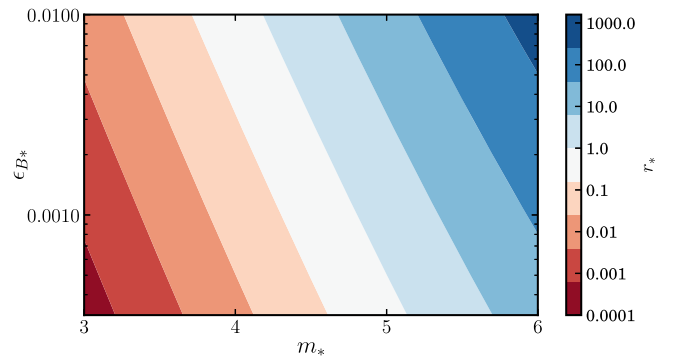


FIG. 1. Peak tensor-to-scalar ratio r_* as a function of ϵ_{B*} and m_* for $k_p = 0.005 \text{ Mpc}^{-1}$.

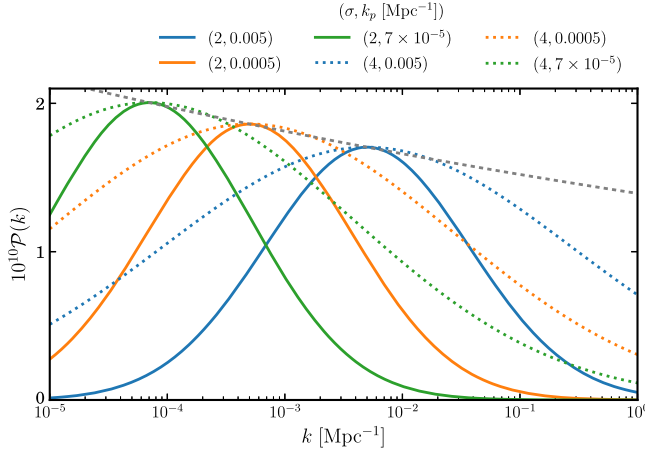


FIG. 2. Predicted tensor spectrum, $\mathcal{P}_h^{\text{L,Sourced}}$, for three sets of parameters: (blue) $\sigma = 2$, $r_* = 0.07$, $k_p = 0.005 \text{ Mpc}^{-1}$, (orange) $\sigma = 2$, $r_* = 0.07$, $k_p = 0.0005 \text{ Mpc}^{-1}$, (green) $\sigma = 2$, $r_* = 0.07$, $k_p = 7 \times 10^{-5} \text{ Mpc}^{-1}$.

the rest of this paper, we model the primordial tensor spectrum as being the sum of two contributions: a completely polarized sourced contribution to the tensor spectrum $\mathcal{P}_h^{\text{Sourced}}$, and a contribution from the vacuum fluctuations, which we take to be unpolarized and which we do not vary:

$$\begin{aligned} \mathcal{P}_h^{\text{vac}} &= A_T \left(\frac{k}{k_*} \right)^{n_T}, \\ \mathcal{P}_\zeta^{\text{vac}} &= A_S \left(\frac{k}{k_*} \right)^{n_S-1}, \end{aligned} \quad (4)$$

where $A_T = r_{\text{vac}} A_S$, $A_S = 2.2 \times 10^{-9}$, $n_S = 0.96$, and $k_* = 0.05 \text{ Mpc}^{-1}$ are taken from the best-fit Planck cosmology [39]. We fix $r_{\text{vac}} = 10^{-5}$, which corresponds to the inflationary Hubble scale $H_{\text{inf}} = 8 \times 10^{11} \text{ GeV}$, and the tensor tilt is given by the consistency relation $n_T = -r_{\text{vac}}/8$. Note that r_{vac} is not required to be so small compared to the sourced contribution; for larger values of r_{vac} , the chiral contribution would be more difficult to detect on the CMB due to the vacuum contribution to the BB spectrum. Therefore, we make the simplifying assumption of a small r_{vac} . In summary,

$$\begin{aligned} \mathcal{P}_\zeta(k) &= \mathcal{P}_\zeta^{\text{vac}}, \\ \mathcal{P}_h(k, k_p, r_*, \sigma) &= \mathcal{P}_h^{\text{vac}}(k) + \mathcal{P}_h^{\text{Sourced}}(k, k_p, r_*, \sigma), \\ \mathcal{P}_h^{\text{L}}(k) - \mathcal{P}_h^{\text{R}}(k) &= \mathcal{P}_h^{\text{Sourced}}(k, k_p, r_*, \sigma). \end{aligned}$$

It is found that, contrary to the tensor perturbation, the scalar perturbations in the axion- $SU(2)$ sector do not have any instability for $m_Q \geq \sqrt{2}$, and they are even suppressed compared to the vacuum fluctuation of a massless scalar field due to their kinetic and mass mixing [13,40,41]. Since the axion- $SU(2)$ sector is decoupled from the inflaton and its energy density is subdominant, its contribution to the

curvature perturbation is negligible. It is possible that the energy fraction of the axion $\Omega_\chi \equiv \rho_\chi/\rho_{\text{total}}$ grows after inflation, and χ becomes a curvaton if σ is very large, and the decay of the axion is suppressed more than that of the inflaton [42–44]. In that case, the contribution from the scalar perturbations in the axion- $SU(2)$ sector to the curvature perturbation may be significant, and hence it would be interesting to investigate such cases. However, it is beyond the scope of this paper. Therefore, we can simply consider that the curvature perturbation produced by the inflaton is not affected by the axion and the $SU(2)$ gauge fields in this model. We may then take the TT, EE, and TE spectra to be given by constrained cosmological parameters (which we take to be $h = 0.675$, $\Omega_b = 0.022$, $\Omega_c = 0.12$, $n_s = 0.96$, $\tau = 0.09$, $A_s = 2.2 \times 10^{-9}$) and investigate only the B-mode spectra: TB, EB, and BB.

III. CMB

In this section, we study the CMB phenomenology of the model introduced in Sec. II. The interesting CMB features of this are the nonzero TB and EB spectra produced by the chiral tensor spectrum. We will calculate the expected TB and EB spectra and make forecasts of their detectability by the LiteBIRD satellite in the presence of cosmic variance, residual foregrounds, instrumental noise, gravitational lensing, and polarimeter self-calibration.

The anisotropies on the CMB are calculated by the integration of the primordial perturbation spectra over the transfer functions describing the evolution of perturbations with time. The tensor contribution to the angular power spectra of the anisotropies are [21,24–26]

$$\begin{aligned} C_\ell^{t,X_1 X_2} &= 4\pi \int d(\ln k) [\mathcal{P}_h^{\text{L}}(k) + \mathcal{P}_h^{\text{R}}(k)] \Delta_{X_1, \ell}^t(k) \Delta_{X_2, \ell}^t(k), \\ C_\ell^{t,Y_1 Y_2} &= 4\pi \int d(\ln k) [\mathcal{P}_h^{\text{L}}(k) - \mathcal{P}_h^{\text{R}}(k)] \Delta_{Y_1, \ell}^t(k) \Delta_{Y_2, \ell}^t(k). \end{aligned} \quad (5)$$

where $X_1 X_2 = \{TT, TE, EE, BB\}$ and $Y_1 Y_2 = \{TB, EB\}$, and $\Delta_{X, \ell}^t(k)$ indicates the tensor transfer function [45]. To calculate these spectra, we use the CLASS code [46], making the necessary modifications for it to calculate TB and EB spectra. In Fig. 3, we plot examples of the BB and TB spectra calculated in this way for a few different combinations of the model parameters and compare them to the noise contributions from lensing, instrument noise, and foreground residuals that we will consider later.

In this paper, we assess the detectability of the chirality of the primordial GWB over the parameter space spanned by (r_*, k_p, σ) . Therefore, we calculate the expected signal-to-noise ratio of the combined TB and EB spectra [19]:

$$\left(\frac{S}{N} \right)_{\text{TB+EB}}^2 = \sum_{\ell=2}^{\ell_{\text{max}}} \sum_{X_1 X_2, X_3 X_4} C_\ell^{X_1 X_2} [\mathcal{E}^{-1}]_\ell^{X_1 X_2 X_3 X_4} C_\ell^{X_3 X_4}, \quad (6)$$

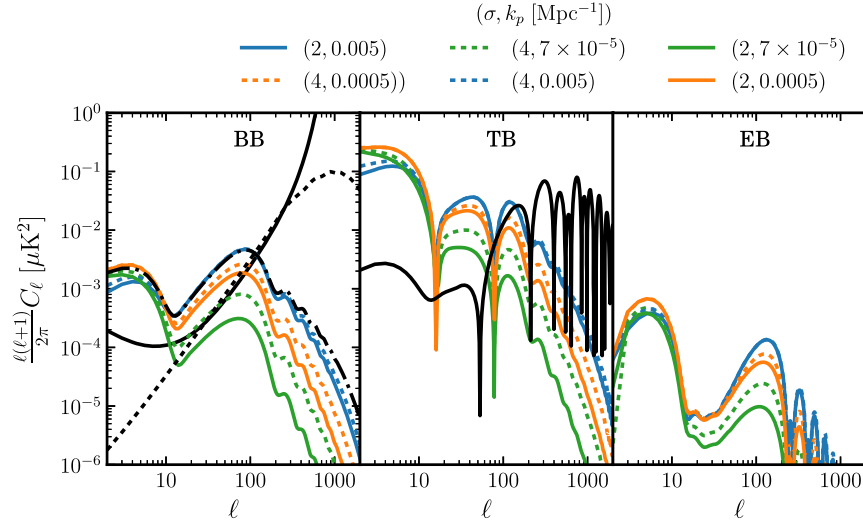


FIG. 3. LEFT PANEL: C_ℓ^{BB} for the same three sets of parameters used in Fig. 2: (blue) $\sigma = 2$, $r_* = 0.07$, $k_p = 0.005 \text{ Mpc}^{-1}$, (orange) $\sigma = 2$, $r_* = 0.07$, $k_p = 0.0005 \text{ Mpc}^{-1}$, (green) $\sigma = 2$, $r_* = 0.07$, $k_p = 7 \times 10^{-5} \text{ Mpc}^{-1}$, compared to the LiteBIRD noise spectrum with 2% foregrounds (solid black), the lensing BB spectrum (dashed black), and the standard vacuum fluctuation $C_\ell^{BB}(r = 0.07)$ consistent with the BKP $r < 0.07$ (95% C.L.) (dash-dot black). The axion- $SU(2)$ spectra contain a contribution from vacuum fluctuations with $r = 10^{-5}$, as is used in the text. RIGHT PANEL: $|C_\ell^{TB}|$ (solid color) and $|C_\ell^{EB}|$ (dashed color) spectra for the same three sets of parameters. Shown in black is an example of the spurious TB signal induced by polarimeter miscalibration for an angle of one arcminute, as discussed in Sec. III C.

where $X_1 X_2, X_3 X_4 = \{TT, EE, BB, TE, TB, EB\}$, and ξ is the covariance of our estimate of the power spectra given a certain theoretical and experimental setup: $\xi^{X_1 X_2 X_3 X_4} = \langle (\hat{C}_\ell^{X_1 X_2} - C_\ell^{X_1 X_2})(\hat{C}_\ell^{X_3 X_4} - C_\ell^{X_3 X_4}) \rangle = \frac{1}{(2\ell+1)f_{\text{sky}}} (\tilde{C}_\ell^{X_1 X_3} \tilde{C}_\ell^{X_2 X_4} + \tilde{C}_\ell^{X_1 X_4} \tilde{C}_\ell^{X_2 X_3})$, where tildes indicate the observed spectrum: $\tilde{C}_\ell^{XX'} = C_\ell^{XX'} + N_\ell^{XX'}$, with $N_\ell^{XX'}$ denoting the noise spectrum, and the calculation of ξ is detailed in Appendix B. ℓ_{max} denotes the highest multipole we consider, which in this case is 500.

Similarly, we can calculate the detectability of the primordial GWB, as opposed to its chirality, by calculating the signal-to-noise ratio of its contribution to the BB spectrum. In the case of no lensing, this is simply

$$\left(\frac{S}{N}\right)_{BB}^2 = f_{\text{sky}} \sum_{\ell=2}^{\ell_{\text{max}}} \frac{(2\ell+1)}{2} \left[\frac{C_\ell^{BB}}{\tilde{C}_\ell^{BB}} \right]^2. \quad (7)$$

However, one of the major sources of uncertainty in a measurement of the BB spectrum is due to gravitational lensing. As the CMB propagates to us from the surface of the last scattering, it is gravitationally lensed by the intervening matter density, converting primary E-mode anisotropies to secondary B-mode anisotropies, which then need to be accounted for in measurements of BB [47].

We can separate the contributions to BB into $C_\ell^{BB} = C_\ell^{BB, \text{Prim}} + C_\ell^{BB, \text{Lens}}$, where “Prim” and “Lens” refer to the primordial and lensed contributions, respectively. We are interested in measuring $C_\ell^{BB, \text{Prim}}$, and in effect, $C_\ell^{BB, \text{Lens}}$ acts as an extra source of noise, with an unknown

amplitude. The modification required to calculate the signal-to-noise ratio of the primordial BB signal is to consider the 2×2 matrix:

$$\mathcal{F}_{ij} = \sum_{\ell=2}^{\ell_{\text{max}}} \frac{(2\ell+1)f_{\text{sky}}}{2} \frac{C_\ell^{BB, i} C_\ell^{BB, j}}{(\tilde{C}_\ell^{BB})^2}, \quad (8)$$

such that

$$\left(\frac{S}{N}\right)_{BB, i}^2 = \frac{1}{(\mathcal{F}^{-1})_{ii}}, \quad (9)$$

where the indices i and j run over “Prim” and “Lens”. Note that we will assume that the temperature spectrum is perfectly known over the range of scales we are interested in and that the sourced contribution to the scalar spectrum is negligible [13]: $\tilde{C}_\ell^{TT} = C_\ell^{TT}$.

A. Cosmic variance limited case

Here, we discuss the signal-to-noise ratio of the TB, EB, and BB spectra in the case of cosmic variance limited observations: $\tilde{C}_\ell^{XX'} = C_\ell^{XX'}$. In this scenario, in the absence of lensing, Eq. (7) has the simple analytic form $(\frac{S}{N})_{BB}^2 = f_{\text{sky}}(\ell_{\text{max}} + 3)(\ell_{\text{max}} - 1)/2$. The signal-to-noise ratios of the TB and EB spectra calculated using Eq. (6) are shown in Fig. 4 for the parameter space of the model, assuming a lensed BB spectrum with $f_{\text{sky}} = 1$. We consider only $r_* < 0.07$, in line with current observational constraints on the scale-invariant tensor-to-scalar ratio

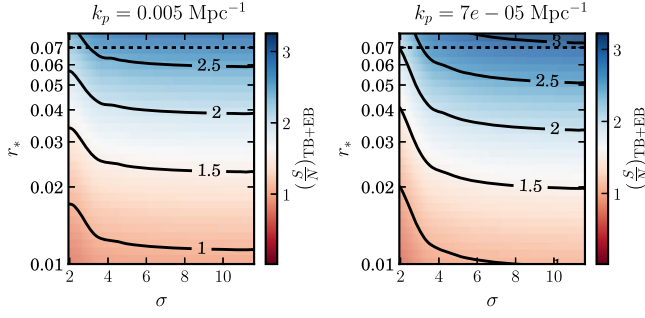


FIG. 4. Signal-to-noise ratio of $TB + EB$ spectra assuming the perfect case of $f_{\text{sky}} = 1$, with no foreground contamination, noiseless observations, and no delensing. The black dashed line indicates the bounds placed by $r_* < 0.07$. LEFT PANEL: $k_p = 5 \times 10^{-3} \text{ Mpc}^{-1}$. RIGHT PANEL: $k_p = 7 \times 10^{-5} \text{ Mpc}^{-1}$.

$r_{0.05} < 0.07$ (95% C.L.), where the subscript indicates the pivot scale in Mpc^{-1} [7]. Figure 3 demonstrates that the shape of C_ℓ^{BB} is strongly dependent on the position of the peak in the GW spectrum, k_p , and also on the width of the peak, σ . Therefore, the BKP bound on r does not simply imply the same bound on r_* ; a small value of k_p and σ could allow a large value of r_* without exceeding the BKP limit, due to the small-scale damping of C_ℓ^{BB} . However, except for the $\mathcal{O}(1)$ underestimation for small k_p , the BKP bound provides a useful guide as to what is allowed by current observations.

The values of $k_p = 7 \times 10^{-5} \text{ Mpc}^{-1}$ and $k_p = 5 \times 10^{-3} \text{ Mpc}^{-1}$ were chosen as they probe different scales to which the CMB is sensitive. $\mathcal{P}_h^{\text{L,Sourced}}(k)$ is more sharply peaked for smaller σ , and so for a given r_* , the signal-to-noise ratio decreases with decreasing σ . As σ increases, the tensor spectrum becomes almost scale invariant over the range of scales accessible with the CMB, and so the signal-to-noise ratio does not depend on σ for large values of σ . Figure 4 shows that the maximum achievable signal-to-noise ratio is ~ 3 , and that the chirality is undetectable with $\frac{S}{N} \lesssim 1$ for $r_* \lesssim 0.01$.

B. Including instrument noise and foreground contamination

We now consider instrument noise and contamination of the spectrum due to imperfect foreground separation and assume that we are unable to perform any “delensing”.

The model we use for the noise spectrum includes the instrument noise in the CMB channels, the residual foregrounds in the final CMB map (assumed to be at a level of 2%, following Refs. [19,34,48,49]) and the instrumental noise from channels used for foreground cleaning that is introduced into the CMB channels by the cleaning process. The details of how we combine these factors to produce a final noise contribution to the measured CMB spectrum, as well as the instrument specifications for LiteBIRD, can be found in Appendix C. In the left panel of Fig. 3, we show the contributions to the BB noise spectrum, N_ℓ^{BB} , from

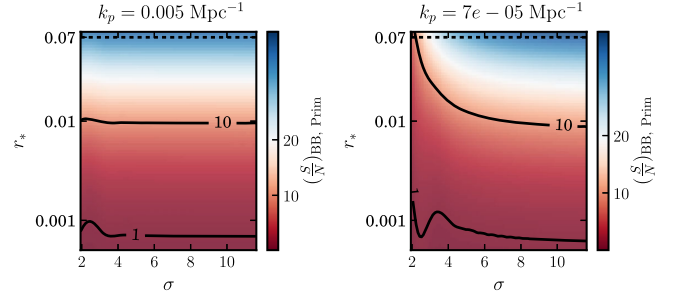


FIG. 5. Signal-to-noise ratio of BB spectrum assuming no delensing and 2% foreground contamination and LiteBIRD instrumental noise added using method described in Appendix C. The dashed line refers to the observational constraint of $r_* = 0.07$. The signal-to-noise ratio achieved in BB is much larger than that in $TB + EB$ as the cosmic variances of BB and TB are proportional to $(C_\ell^{BB})^2$, and $C_\ell^{BB} C_\ell^{TT}$, respectively. The factor of C_ℓ^{TT} means cosmic variance in the TB spectrum is much more significant than that in BB. LEFT PANEL: $k_p = 5 \times 10^{-3} \text{ Mpc}^{-1}$. RIGHT PANEL: $k_p = 7 \times 10^{-5} \text{ Mpc}^{-1}$.

lensing, LiteBIRD instrumental noise, and foreground residuals compared to the primordial C_ℓ^{BB} .

1. BB signal-to-noise ratio

We calculate Eq. (9) over the available parameter space and show the result in Fig. 5. In a similar way to the TB and EB signal-to-noise ratio, we see that there is some dependence on σ , especially in the case of smaller k_p . This is expected since $k_p = 7 \times 10^{-5} \text{ Mpc}^{-1}$ is slightly smaller than those scales to which we expect the CMB to be sensitive [20]. Therefore, we expect that reducing σ for this value of k_p will eventually exclude the tensor perturbations from contributing to CMB scales, explaining the sharp decrease in S/N for low σ and a given r_* . From Fig. 5, it is clear that we can detect the primordial contribution to BB for $r_* > 10^{-3}$, which is consistent with the aim of LiteBIRD to achieve an uncertainty on the null case of $r = 0$ of less than 10^{-3} .

2. TB + EB signal-to-noise ratio

Lensing affects the TB and EB signal-to-noise ratio only through \tilde{C}_ℓ^{BB} , since the direct lensing contributions to TB and EB are negligible [19,24]. We calculate Eq. (6) over the available parameter space, now including instrument noise for a LiteBIRD-type experiment (with parameters shown in Table I), foreground residuals, and gravitational lensing and show the result in Fig. 6. Over the allowed parameter space, the maximum achievable signal-to-noise ratio is $\frac{S}{N} \sim 2$. For $r_* \lesssim 0.03$, LiteBIRD cannot detect chirality in this model, compared to $r_* \lesssim 0.01$ in the CV-limited case. The right panel of Fig. 3 demonstrates that the TB and EB signal peaks at $\ell \lesssim 10$, making the large-scale foreground residual contribution to the noise, shown in the left panel of Fig. 3, the dominant factor causing this reduction in sensitivity.

TABLE I. Summary of the LiteBIRD specifications ($f_{\text{sky}} = 0.5$).

Channel (GHz)	θ_{FWHM} (amin)	$\sigma_p(\nu)$ [$\mu\text{K amin}$]
40.0	69.0	36.8
50.0	56.0	23.6
60.0	48.0	19.5
68.0	43.0	15.9
78.0	39.0	13.3
89.0	35.0	11.5
100.0	29.0	9.0
119.0	25.0	7.5
140.0	23.0	5.8
166.0	21.0	6.3
195.0	20.0	5.7
235.0	19.0	7.5
280.0	24.0	13.0
337.0	20.0	19.1
402.0	17.0	36.9

Improvements in foreground cleaning algorithms could reduce the level of foreground contamination and perhaps allow a larger sky fraction to be used in the analysis. However, even with perfect control of these factors, the cosmic variance limit of Fig. 4 cannot be beaten. We conclude from this study that the most important factor limiting the sensitivity of CMB observations to the chirality of the GWB is the large cosmic variance of the TB and EB spectra due to large scalar T and E signals, respectively.

C. Simultaneous detection and self-calibration

In order to achieve its baseline performance target, LiteBIRD will require an uncertainty on the polarimeter calibration angle of less than one arcminute [50,51]. There are several methods that have been used in the past to calibrate polarimeters such as polarized astrophysical sources like the Crab Nebula (Tau A) or man-made sources such as a polarization selective mesh. There are many

factors preventing such methods achieving calibrations better than one degree. For example, Tau A is the best candidate for a pointlike polarized source, but this provides a calibration uncertainty of ~ 0.5 degrees [52], and with these, it is hard to achieve a calibration uncertainty better than one degree [53]. The polarization of Tau A also has a poorly understood frequency dependence and is ultimately an extended source, making it poorly suited to a characterization of the polarized beam [54]. Man-made sources, on the other hand, must often be placed in the near field and are unstable over long time frames. However, a recent proposal of a balloon-borne artificial polarization source in the far field of ground-based experiments may ameliorate this problem for ground-based telescopes [54].

LiteBIRD plans to self-calibrate its polarimeter using the EB spectrum, which is assumed to have zero contribution from primordial perturbations [55]. Unfortunately, this makes assumptions about cosmology and uses part of the constraining power to calibrate the instrument, instead of for science. Furthermore, residual foreground contributions to TB and EB may result in a biasing of the calibration angle. Reference [56] shows that a miscalibration angle of 0.5 degrees can result in a bias in the recovered value of r of 2×10^{-3} , which is significant for LiteBIRD's aim to push constraints on r to $r \sim 10^{-3}$. However, Ref. [56] also finds that TB and EB are consistent with zero in a study of the low-foreground BICEP2 region. Furthermore, in a study of the Planck data, Ref. [57] finds that TB and EB are both consistent with zero for sky fractions up to $f_{\text{sky}} = 0.3$, and that TB increases to significant levels only for larger sky fractions, while EB is only marginally nonzero for $f_{\text{sky}} = 0.7$. Therefore, while foregrounds must be considered, they do not necessarily limit the use of this approach to calibration.

We want to study the detectability of primordial TB and EB correlations when taking self-calibration into account. The self-calibration process is carried out by zeroing the miscalibration $\Delta\psi$ by measuring its contribution to the TB and EB spectra. In this analysis, we will assume that residual foreground contributions to TB and EB are negligible.

If the angle of the polarimeter is miscalibrated by some angle $\Delta\psi$, the measured Q and U will be rotated. We work with the spin-2 quantities $(Q \pm iU)(\hat{n})$, which have the transformation properties under rotation:

$$(\tilde{Q} \pm i\tilde{U})(\hat{n}) = e^{\pm i2\Delta\psi}(Q \pm iU)(\hat{n}).$$

E and B can be computed to find

$$\begin{pmatrix} \tilde{a}_{\ell m}^T \\ \tilde{a}_{\ell m}^E \\ \tilde{a}_{\ell m}^B \end{pmatrix} = \begin{pmatrix} 1 & 0 & 0 \\ 0 & \cos(2\Delta\psi) & -\sin(2\Delta\psi) \\ 0 & \sin(2\Delta\psi) & \cos(2\Delta\psi) \end{pmatrix} \begin{pmatrix} a_{\ell m}^T \\ a_{\ell m}^E \\ a_{\ell m}^B \end{pmatrix}$$

which give the resulting rotations of the angular power spectra:

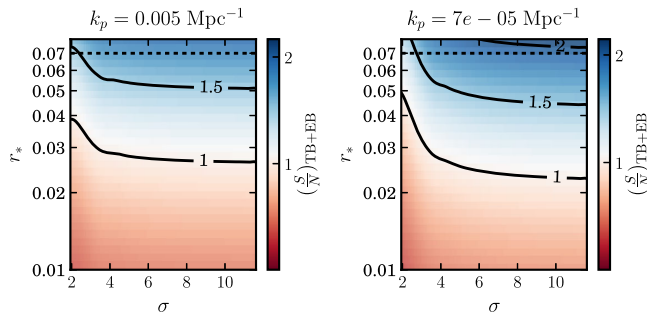


FIG. 6. Signal-to-noise ratio of $TB + EB$ spectra assuming no delensing and 2% foreground contamination and LiteBIRD instrumental noise added using method described in Appendix C. The dashed line refers to the observational constraint of $r_* = 0.07$. LEFT PANEL: $k_p = 5 \times 10^{-3} \text{ Mpc}^{-1}$. RIGHT PANEL: $k_p = 7 \times 10^{-5} \text{ Mpc}^{-1}$.

$$\begin{pmatrix} C_\ell^{TE} \\ C_\ell^{TB} \\ C_\ell^{EE} \\ C_\ell^{BB} \\ C_\ell^{EB} \end{pmatrix}_{\text{rot}} = \begin{pmatrix} \cos(2\Delta\psi) & -\sin(2\Delta\psi) & 0 & 0 & 0 \\ \sin(2\Delta\psi) & \cos(2\Delta\psi) & 0 & 0 & 0 \\ 0 & 0 & \cos^2(2\Delta\psi) & \sin^2(2\Delta\psi) & -\sin(4\Delta\psi) \\ 0 & 0 & \sin^2(2\Delta\psi) & \cos^2(2\Delta\psi) & \sin(4\Delta\psi) \\ 0 & 0 & \frac{\sin(4\Delta\psi)}{2} & -\frac{\sin(4\Delta\psi)}{2} & \cos(4\Delta\psi) \end{pmatrix} \begin{pmatrix} C_\ell^{TE} \\ C_\ell^{TB} \\ C_\ell^{EE} \\ C_\ell^{BB} \\ C_\ell^{EB} \end{pmatrix}. \quad (10)$$

We then replace the primordial spectra in our expression for \tilde{C}_ℓ with the rotated spectra:

$$\tilde{C}_\ell^{XX'} = C_{\text{rot}}^{XX'} + N_\ell^{XX'}.$$

We jointly estimate the uncertainty on the miscalibration angle and the recovered amplitude of the TB and EB spectra parametrized by r_* using the Fisher information:

$$\mathcal{F}_{ij} = \sum_{X_1 X_2, X_3 X_4} \sum_{\ell=2}^{\ell_{\text{max}}} \frac{\partial C_\ell^{X_1 X_2}}{\partial a_i} [\xi^{-1}]^{X_1 X_2 X_3 X_4} \frac{\partial C_\ell^{X_3 X_4}}{\partial a_j} \quad (11)$$

where $a_i, a_j = \Delta\psi, r_*$. The uncertainty on the miscalibration angle is then given by $(\sigma_{\Delta\psi})^2 = (\mathcal{F}^{-1})_{\Delta\psi \Delta\psi}$. We can easily calculate the derivatives with respect to $\Delta\psi$ in Eq. (11) using Eq. (10). In order to calculate the derivatives with respect to r_* , we write $C_\ell^{TB/EB} = r_* C_\ell^{TB/EB}(r_* = 1)$. In order to study the interaction of the miscalibration angle and primordial chirality, we calculate the correlation coefficient:

$$\alpha \equiv \frac{\mathcal{F}_{\Delta\psi r_*}}{\sqrt{\mathcal{F}_{\Delta\psi \Delta\psi} \mathcal{F}_{r_* r_*}}}.$$

We now calculate the 1- σ uncertainty in a measurement of the miscalibration angle $\Delta\psi$ and α over the allowed parameter space of the model and show the resulting contour plots in Fig. 7.

We find that for LiteBIRD, $\sigma_{\Delta\psi} < 1$ arcmin for all of the allowed space, making the simultaneous calibration of the polarimeter and detection of the parity violation possible. The correlation coefficient is less than 0.03 for the allowed parameter space, indicating that the effects of primordial

parity violation and miscalibration are easily separable. This can be understood from the right panel of Fig. 3, where it is clear that the primordial signal is a large-scale effect, with maximum signal at $\ell \sim 10$, whereas the contribution to TB from miscalibration is a small-scale effect which dominates at $\ell > 100$. This is supported by the σ dependence of α in the left panel of Fig. 7. The two effects become more correlated for larger values of σ , which correspond to flatter spectra and hence more power at small scales. Varying k_p has little effect on the result that the effects are separable but does introduce some interesting dependence on σ . This indicates that a sufficiently high ℓ_{max} is necessary for the separation of these effects. For smaller values of k_p , $\sigma_{\Delta\psi}$ becomes more dependent on σ . For example, with $k_p = 7 \times 10^{-5} \text{ Mpc}^{-1}$, for a given r_* , $\sigma_{\Delta\psi}$ increases with σ since the flatter spectra of large σ become more important when k_p is further away from the small scales at which the miscalibration effect occurs. On the other hand, when $k_p = 5 \times 10^{-3} \text{ Mpc}^{-1}$, the dependence on σ is reversed. This is because the miscalibration effect peaks at $\ell \sim 100$, which corresponds to contributions from modes around $k \sim 100/\eta_0 = 7 \times 10^{-3} \text{ Mpc}^{-1}$, where η_0 is the comoving distance to the surface of last scattering. Therefore, an increase of σ for $k_p \sim 7 \times 10^{-3} \text{ Mpc}^{-1}$ will make the signals less correlated as the flatter spectra will introduce more power at larger scales.

In conclusion, any reduction in sensitivity to TB and EB due to the calibration requirements is negligible and is ignored in the results we quote for LiteBIRD. Our results are in agreement with Refs. [25,36], which also find that the primordial and miscalibration contributions are readily separable.

D. CMB results

Here, we summarize the findings of the CMB section and provide a prognosis of the usefulness of CMB observations in detecting gravitational wave chirality.

In the case of cosmic variance limited ultimate observations, we found that over the parameter space of the model the maximum signal-to-noise ratio achievable was ~ 3 for the largest values of r_* , and that the chirality is undetectable for $r_* \lesssim 0.01$, in agreement with previous studies of simpler models of chiral GWBs with nearly scale-invariant spectra [24–26]. Moving on to the realistic case of a LiteBIRD-like experiment with no delensing capability, a 2% level of foreground residuals, and a

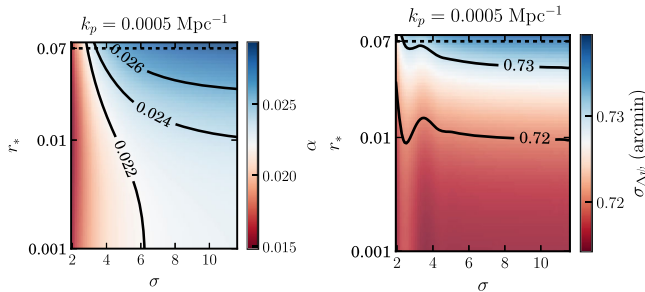


FIG. 7. Correlation coefficient α (left) and 1- σ uncertainty on the polarimeter calibration (right) for LiteBIRD, calculated over the allowed parameter space of the model assuming 2% foreground residual and no delensing. The dashed line shows the observational constraint of $r_* = 0.07$.

simultaneous self-calibration, we find that for the largest allowable values of r_* it may achieve a signal-to-noise ratio of 2.0, making the chirality detectable. The chirality is undetectable by LiteBIRD for $r_* \lesssim 0.03$.

Though a detection with a 2-sigma significance may be of interest, it is only achievable for a small part of the parameter space, $0.03 \lesssim r_* \lesssim 0.07$, and in any event, we have demonstrated that we may not exceed a $\frac{S}{N}$ of 3 using CMB two-point statistics. We also investigated a CORe+ design with the same level of foreground residuals as LiteBIRD and found that it is performed very similarly to LiteBIRD since both instruments would be limited by foreground residuals on the large scales we are interested in. As stated in Sec. I, we will not gain anything extra from Stage 4 observations, as they are limited to $\ell \gtrsim 30$. Therefore, in order to make stronger statistical detections of this model using the CMB, higher order statistical techniques taking advantage of the model's non-Gaussianity may have more success as shown for the axion- $U(1)$ model [19].

Alternatively, we can investigate different physical probes altogether. In the next section, we consider complementary constraints on the axion- $SU(2)$ model from space-based laser interferometer gravitational wave observatories.

IV. LASER INTERFEROMETERS

Due to the strong scale dependence of the tensor spectrum, it may be possible to study the case of large k_p using laser interferometer gravitational wave observatories. Previous studies have indicated that the scale-invariant spectrum of single-field slow-roll inflation would be too weak at interferometer scales to be detected by current generation interferometers such as LIGO [58], VIRGO [59], and LISA [38]. However, the model we consider has a large feature at k_p ; therefore, for $k_p \sim 10^{11} - 10^{13} \text{ Mpc}^{-1}$, current generation interferometers may be sensitive to the GWB of the axion- $SU(2)$ model.

It should be noted that it is difficult to have a sourced gravitational wave spectrum with a sharp peak on interferometer scales. This is because of the attractor behavior of the background axion field coupled to the $SU(2)$ gauge fields (see Appendix A). As a result, we consider the rather flat spectra seen in Fig. 8. For such flat spectra, one may expect any signal detectable with interferometers would also be detectable on CMB scales, making the use of interferometers redundant. We therefore first demonstrate the complementarity of our CMB and interferometer studies. We compare their sensitivities as a function of the frequency f of the gravitational wave background. The quantity we use to compare sensitivities is the minimum detectable fractional energy density in primordial gravitational waves:

$$\Omega_{\text{GW}}(f) \equiv \frac{1}{\rho_c} \frac{\partial \rho_{\text{GW}}}{\partial \ln(f)}, \quad (12)$$

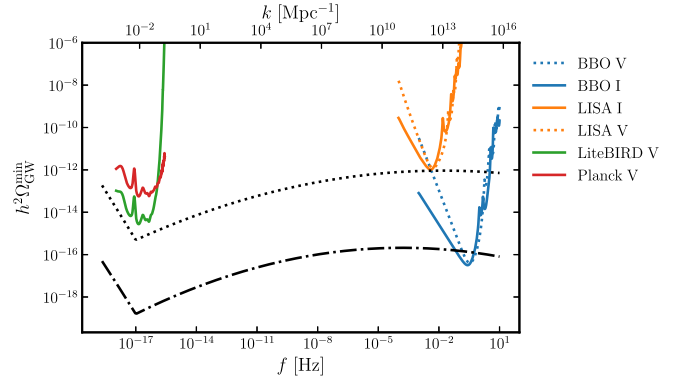


FIG. 8. Comparison of the sensitivity curves for LiteBIRD, Planck, LISA, and BBO corresponding to a signal-to-noise ratio of 1 at a given frequency in intensity (I) or polarization (V). At the top horizontal axis, we also show the corresponding wave-number computed via $\frac{k}{\text{Mpc}^{-1}} = 6.5 \times 10^{14} \frac{f}{\text{Hz}}$. Also plotted are the primordial spectra for the parameters: $k_p = 10^{13} \text{ Mpc}^{-1}$, $\sigma = 9$, $r_* = 835$ (black dotted), and $k_p = 10^{11} \text{ Mpc}^{-1}$, $\sigma = 8$, $r_* = 0.15$ (black dash-dotted). Note that below $f = 10^{-17} \text{ Hz}$, transfer function of the fractional gravitational wave background energy density changes due to the transition between matter and radiation-dominated eras. We see that even for the large values of σ required by the large k_p values of the axion- $SU(2)$ model LISA and BBO can make a detection that would still be inaccessible at CMB scales. This motivates the evaluation of signal-to-noise ratio for the interferometers. Note that the CMB sensitivity curves have been smoothed with a Gaussian kernel due to the sharp oscillations introduced by the transfer function [Eq. (D2)].

where ρ_c is the critical density to close the Universe evaluated today, and $\rho_{\text{GW}} = \frac{c^2}{32\pi^2 G} \langle h_{ij} h_{ij} \rangle$, where $h_{ij} \equiv \delta g_{ij}^{TT}/a^2$. The calculation for the CMB is detailed in Appendix D and for interferometers in the remainder of this section. Figure 8 displays the minimum detectable fractional energy density using the CMB and interferometers for Planck, LiteBIRD, an advanced LISA [38], and BBO [60]. We see that LiteBIRD has a much improved sensitivity to chirality, compared to Planck, which is due to its much lower instrumental noise. The two plotted theoretical spectra are clearly detectable by LISA or BBO, without being detectable at CMB scales, making interferometers an independent, complementary probe of the primordial spectrum of the axion- $SU(2)$ model.

A. Interferometer notation

Laser interferometers consist of a set of test masses placed at nodes and linked by laser beams. Interferometry is used to measure the change in the optical path length between test masses. A passing gravitational wave induces a time-dependent oscillation in the optical path length, which can be isolated from noise by taking cross-correlations between detectors.

The metric perturbation at point \mathbf{x} at time t , $h_{ij}(t, \mathbf{x})$, can be decomposed into a superposition of plane waves [61]:

$$h_{ij}(t, \mathbf{x}) = \sum_P \int d^3\mathbf{k} C_P(\mathbf{k}) \times \sin(ckt - \mathbf{k} \cdot \mathbf{x} + \Phi(k)) e_{ij}^P(\hat{\Omega}),$$

where we use the transverse traceless basis tensors with normalization $e_{ij}^P(\hat{\Omega}) e_{ij}^{P'}(\hat{\Omega}) = 2\delta_{PP'}$, and $P = +, \times$. It is more convenient to deal with complex values, and so we rewrite this as

$$h_{ij}(t, \mathbf{x}) = \sum_P \int_{-\infty}^{\infty} df \int d^2\hat{\Omega} h_P(f, \hat{\Omega}) \times \exp\left(2\pi i f \left(t - \frac{\mathbf{x} \cdot \hat{\Omega}}{c}\right)\right) e_{ij}^P(\hat{\Omega}),$$

where $ck = 2\pi f$, $\mathbf{k} \cdot \mathbf{x} = 2\pi f \frac{\hat{\Omega} \cdot \mathbf{x}}{c}$, and $\hat{\Omega}$ is a unit vector in the direction of propagation of the gravitational wave. Since the coefficients satisfy $h_P(f, \hat{\Omega}) = h_P^*(-f, \hat{\Omega})$, $h_{ij}(t, \mathbf{x})$ is explicitly real. The theory we are dealing with produces a highly non-Gaussian GWB [62]. We can summarize the two-point statistics using the following expectation values of the Fourier coefficients, but this will not capture all the available information:

$$\begin{aligned} & \langle h_P(f, \hat{\Omega}) h_{P'}^*(f', \hat{\Omega}') \rangle \\ &= \frac{1}{2} \delta(f - f') \frac{\delta^{(2)}(\hat{\Omega} - \hat{\Omega}')}{4\pi} S_h^{PP'}(f), \\ & \times \begin{pmatrix} \langle h_+(f, \hat{\Omega}) h_+^*(f', \hat{\Omega}') \rangle & \langle h_+(f, \hat{\Omega}) h_\times^*(f', \hat{\Omega}') \rangle \\ \langle h_\times(f, \hat{\Omega}) h_+^*(f', \hat{\Omega}') \rangle & \langle h_\times(f, \hat{\Omega}) h_\times^*(f', \hat{\Omega}') \rangle \end{pmatrix} \\ &= \frac{1}{2} \delta(f - f') \frac{\delta^{(2)}(\hat{\Omega} - \hat{\Omega}')}{4\pi} \begin{pmatrix} I(f) & iV(f) \\ -iV(f) & I(f) \end{pmatrix}, \end{aligned} \quad (13)$$

where $I(f)$ and $V(f)$ are the Stokes parameters for intensity and circular polarization, respectively. As shown below, $V(f)$ quantifies the difference between the amplitudes of two circular polarization states and hence is a clean observable for the chiral GWB [30–32].

B. Interferometer response

In this section, we present the design of the interferometers for which we will forecast the sensitivity to a polarized gravitational wave background. This analysis uses the designs proposed by Ref. [33]. We summarize some of the results of Ref. [33] here; however, for further details, we refer readers to Ref. [33].

Let us consider a set of masses placed at positions \mathbf{x}_i and the phase change, $\Delta\phi_{ij}$, of light as it travels from mass i at time t_i to mass j arriving at time t [63]:

$$\begin{aligned} \Delta\phi_{ij}(t) &= \int_{-\infty}^{\infty} df \int d^2\hat{n} \sum_P \tilde{h}_P(f, \hat{n}) e_{ab}^P(\hat{n}) \\ &\times e^{i2\pi f(t_i - \hat{n} \cdot \mathbf{x}_i)} D^{ab}(\hat{u}_{ij} \cdot \hat{n}, f), \end{aligned} \quad (14)$$

where D^{ab} is the single-arm transfer function which contains all the geometric information about the instrument and must be derived individually for each interferometer setup [64], and \hat{u}_{ij} is a unit vector pointing from detector i to detector j . We now define the Fourier transform of a signal $g(t)$ observed for a time T : $g(f) = \int_{-T/2}^{T/2} g(t) \exp(-2\pi i f t) dt$. The Fourier transform of the phase change $\Delta\phi$ is then

$$\begin{aligned} \Delta\phi_{ij}(f) &= \int_{-T/2}^{T/2} dt \int_{-\infty}^{\infty} df' \int d^2\hat{\Omega} \sum_P h_P(f', \hat{\Omega}) \\ &\times \exp\left(i2\pi f' \left(t - \frac{\mathbf{x} \cdot \hat{\Omega}}{c}\right) - 2\pi i f t\right) D^{ab}(\hat{u}_{ij} \cdot \hat{n}, f') \\ &= \int_{-\infty}^{\infty} df' \delta_T(f - f') \int d^2\hat{\Omega} \sum_P h_P(f', \hat{\Omega}) \\ &\times \exp\left(-i2\pi f' \frac{\mathbf{x} \cdot \hat{\Omega}}{c}\right) D^{ab}(\hat{u}_{ij} \cdot \hat{n}, f'), \end{aligned} \quad (15)$$

where δ_T is a finite-time approximation to the delta function defined as $\delta_T(f - f') \equiv T \text{sinc}(\pi T(f - f'))$, with the properties $\delta_T(0) = T$, $\lim_{T \rightarrow \infty} \delta_T(f) \rightarrow \delta(f)$. We may form a signal by constructing a linear combination of phase changes along different paths around the instrument and then cross-correlating these signals. The signal we seek to measure is stochastic, and so to distinguish it from noise, we must cross-correlate the detector output with the output from a detector with independent noise properties. The expectation of the cross-correlated signal will be composed of terms like

$$\begin{aligned} & \langle \Delta\phi_{ij}(f_1) \Delta\phi_{kl}(f_2) \rangle \\ &= \int_{-\infty}^{\infty} df' \int_{-\infty}^{\infty} df'' \int d^2\hat{\Omega}_1 \int d^2\hat{\Omega}_2 \\ &\times \sum_{P_1 P_2} \delta_T(f_1 - f') \delta_T(f_2 - f'') \langle h_{P_1}(f', \hat{\Omega}_1) h_{P_2}(f'', \hat{\Omega}_2) \rangle \\ &\times \exp(-2\pi i f' t \hat{\Omega}_1 \cdot \mathbf{x}_i) \exp(-2\pi i f'' t \hat{\Omega}_2 \cdot \mathbf{x}_k) \\ &\times D^{ab}(\hat{u}_{ij} \cdot \hat{\Omega}_1, f') D^{cd}(\hat{u}_{kl} \cdot \hat{\Omega}_2, f'') e_{ab}^{P_1}(\hat{\Omega}_1) e_{cd}^{P_2}(\hat{\Omega}_2). \end{aligned} \quad (16)$$

Using $\langle h_{P_1}(f', \hat{\Omega}_1) h_{P_2}(f'', \hat{\Omega}_2) \rangle = \langle h_{P_1}(f', \hat{\Omega}_1) h_{P_2}^*(-f'', \hat{\Omega}_2) \rangle$ and $D^{ab}(\hat{u}_{ij} \cdot \hat{\Omega}, -f) = D^{ab*}(\hat{u}_{ij} \cdot \hat{\Omega}, f)$, we can write this as

$$\begin{aligned} & \langle \Delta\phi_{ij}(f_1) \Delta\phi_{kl}(f_2) \rangle \\ &= \frac{1}{2} \int_{-\infty}^{\infty} df' \delta_T(f_1 - f') \delta_T(f_2 - f') \\ &\times S_h^{P_1 P_2}(f') \mathcal{R}_{P_1 P_2}^{ijkl}(f'), \\ &\mathcal{R}_{P_1 P_2}^{ijkl}(f) \\ &= \frac{1}{4\pi} \int d^2\hat{\Omega} \exp(-2\pi i f \hat{\Omega} \cdot (\mathbf{x}_i - \mathbf{x}_k)) \\ &\times D^{ab}(\hat{u}_{ij} \cdot \hat{\Omega}, f) D^{cd}(\hat{u}_{kl} \cdot \hat{\Omega}, f) e_{ab}^{P_1}(\hat{\Omega}_1) e_{cd}^{P_2}(\hat{\Omega}). \end{aligned} \quad (17)$$

Here, $\mathcal{R}_{P_i P_j}^{ijkl}$ is referred to as the response function of the detector. \mathcal{R} depends on the relative position and orientation of the arms $i \rightarrow j$ and $k \rightarrow l$, as well as the transfer functions of the two arms.

In the remainder of this section, we consider two interferometer designs. In Sec. IV B 1, we consider the baseline design for near-future space-based interferometers such as the European Space Agency-led Laser Interferometer Space Antenna (LISA) [37], and in Sec. IV B 2, we consider two futuristic “advanced stage” LISA-like missions similar to the proposed Big Bang Observatory (BBO) [60].

1. One constellation

In this section, we consider the design shown in the left panel of Fig. 9. This is the baseline design of the LISA mission and consists of three satellites placed at the vertices \mathbf{x}_i of an equilateral triangle of side L and a total of six laser links between the satellites, allowing for measurement of the phase change $\Delta\phi_{ij}$, where $i, j = \{1, 2, 3\}, i \neq j$. We define the following three signals:

$$\begin{aligned} s^\alpha(t) &= \frac{1}{2}(\Delta\phi_{12}(t-2L) + \Delta\phi_{21}(t-L) - \Delta\phi_{13}(t-2L) \\ &\quad - \Delta\phi_{31}(t-L)) + n^\alpha(t), \\ s^\gamma(t) &= \frac{1}{2}(\Delta\phi_{31}(t-2L) + \Delta\phi_{13}(t-L) - \Delta\phi_{32}(t-2L) \\ &\quad - \Delta\phi_{23}(t-L)) + n^\gamma(t), \\ s^\beta(t) &= s^\alpha(t) + 2s^\gamma(t). \end{aligned} \quad (18)$$

The equilateral design means that the laser phase noise, which is the dominant contribution to the noise terms $n(t)$, cancels [64]. Furthermore Ref. [33] shows that signals α and β have independent noise properties. We therefore consider their cross-correlations:

$$\begin{aligned} F_X^P(f, \hat{\Omega} \cdot \hat{u}) &= D_{ij}^X(f, \hat{u} \cdot \hat{\Omega}) e_{ij}^P(\hat{\Omega}), \\ D^\alpha(f, \hat{u} \cdot \hat{\Omega}) &= \frac{1}{2} \exp(-2\pi i f \hat{\Omega} \cdot \mathbf{x}_1) [\hat{u} \otimes \hat{u} T_{\text{MI}}(f, \hat{n} \cdot \hat{u}) - \hat{v} \otimes \hat{v} T_{\text{MI}}(f, \hat{\Omega} \cdot \hat{v})], \\ D^\beta(f, \hat{u} \cdot \hat{\Omega}) &= D^\alpha(f, \hat{u} \cdot \hat{\Omega}) + \exp(-2\pi i f \hat{n} \cdot \mathbf{x}_3) [\hat{u} \otimes \hat{u} T_{\text{MI}}(f, \hat{\Omega} \cdot -\hat{u}) - \hat{w} \otimes \hat{w} T_{\text{MI}}(f, \hat{\Omega} \cdot -\hat{w})], \\ T_{\text{MI}}(f, \hat{\Omega} \cdot \hat{u}) &= \frac{1}{2} \left[\text{sinc}\left(\frac{f(1 - \hat{u} \cdot \hat{\Omega})}{2f_*}\right) \exp\left(-i \frac{f}{2f_*} (3 + \hat{u} \cdot \hat{\Omega})\right) + \text{sinc}\left(\frac{f(1 + \hat{u} \cdot \hat{\Omega})}{2f_*}\right) \exp\left(-i \frac{f}{2f_*} (1 + \hat{u} \cdot \hat{\Omega})\right) \right]. \end{aligned}$$

Consider the instrument’s response to a gravitational wave traveling in the direction $\hat{\Omega} = (\theta, \phi)$ and another traveling in a direction with $\theta \rightarrow \pi - \theta$, i.e., reflected in the x - y plane. Since the vectors $\hat{u}, \hat{v}, \hat{w}, \mathbf{x}_i$ are all in the x - y plane, it is easy to see that the products $\mathbf{x} \cdot \hat{\Omega}, \hat{u} \cdot \hat{\Omega}$, etc. are invariant. Under this transformation, only the z part of the basis tensor $e_{ab}^+(\hat{\Omega})$ is altered. Since $D^{ab}(f, \hat{\Omega} \cdot \hat{u})$ is

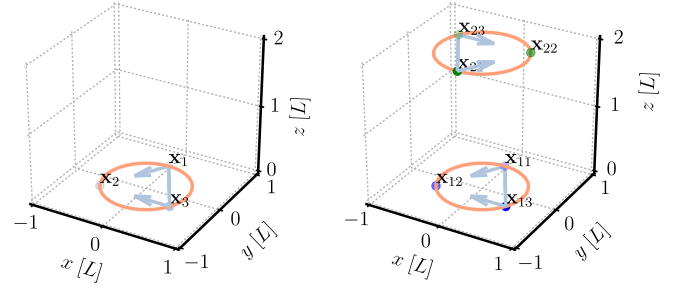


FIG. 9. Possible designs for future space-based laser interferometers. The blue arrows show the laser links used in the Michelson interferometer signals defined in Eq. (18). LEFT PANEL: One constellation design of a space-based interferometer; this corresponds to the baseline LISA design. The points \mathbf{x}_i show the i th satellite. RIGHT PANEL: Advanced stage design of LISA or BBO with two constellations. The points \mathbf{x}_{ij} show the j th satellite on the i th constellation.

$$\begin{aligned} \langle s^{X_1}(f) s^{X_2}(f') \rangle &= \frac{1}{2} \delta(f - f') [\mathcal{R}_I^{X_1 X_2}(f) I(f) \\ &\quad + \mathcal{R}_V^{X_1 X_2}(f) V(f)], \end{aligned} \quad (19)$$

where $X_1, X_2 = \{\alpha, \beta\}$ and

$$\begin{aligned} \mathcal{R}_I^{X_1 X_2}(f) &= \frac{1}{4\pi} \int d^2 \hat{\Omega} [F_{X_1}^+(f, \hat{u} \cdot \hat{\Omega}) F_{X_2}^{+*}(f, \hat{u} \cdot \hat{\Omega}) \\ &\quad + F_{X_1}^\times(f, \hat{u} \cdot \hat{\Omega}) F_{X_2}^{\times*}(f, \hat{u} \cdot \hat{\Omega})], \\ \mathcal{R}_V^{X_1 X_2}(f) &= \frac{1}{4\pi} \int d^2 \hat{\Omega} [F_{X_1}^+(f, \hat{u} \cdot \hat{\Omega}) F_{X_2}^{\times*}(f, \hat{u} \cdot \hat{\Omega}) \\ &\quad - F_{X_1}^\times(f, \hat{u} \cdot \hat{\Omega}) F_{X_2}^{+*}(f, \hat{u} \cdot \hat{\Omega})], \end{aligned} \quad (20)$$

and [33,64,65]

nonzero only in the x - y part, then the product $D^{ab}(f, \hat{\Omega} \cdot \hat{u}) e_{ab}^+(\hat{\Omega})$ is invariant. On the other hand, the x - y part of the $e_{ab}^\times(\hat{\Omega})$ tensor changes sign, meaning that $D^{ab}(f, \hat{\Omega} \cdot \hat{u}) e_{ab}^\times(\hat{\Omega})$ changes sign. Therefore, when performing the angular integral in Eq. (20), the terms with a single power of $F_X^\times(f, \hat{\Omega} \cdot \hat{u})$ go to zero, giving $\mathcal{R}_V^{X_1 X_2}(f) = 0$. The conclusion is that coplanar detectors are not sensitive to the circular polarization of the gravitational wave

background. This is true of other types of detectors with planar geometries such as pulsar timing arrays and individual ground-based detectors such as LIGO [58].

To gain sensitivity to circular polarization, we need to introduce noncoplanar detector arms. Others [31] have considered using cross-correlations between ground-based detectors like LIGO, VIRGO [59], and KAGRA [66], which have a suitable geometry. In the next subsection, we consider an extension to LISA in which we add a second constellation of three satellites to break the coplanar geometry.

2. Two constellations

The extended LISA setup is shown in the right panel of Fig. 9. It consists of two constellations of three equal-arm detectors. The two constellations are separated by a rotation of π radians and a translation of $DL\hat{z}$. The j th detector on the i th constellation is at position \mathbf{x}_{ij} , and the unit vectors joining them are given by $u_i = (\mathbf{x}_{i2} - \mathbf{x}_{i1})/L$, $v_i = (\mathbf{x}_{i3} - \mathbf{x}_{i1})/L$, $w_i = (\mathbf{x}_{i3} - \mathbf{x}_{i2})/L$. We base this analysis on the designs proposed by Ref. [33], which optimize the parameters L and D to achieve equal sensitivity to intensity and polarization of the gravitational wave background. Similar designs have also been considered by [60,64,67].

We use the signals defined in Eq. (18), but α, β are now written α_i, β_i where i refers to the constellation on which we are measuring the signal. The detector transfer functions are the same as the single constellation, but with extra indices referring to the constellation we are considering [33,64]:

$$\begin{aligned} D^{\alpha_i}(f, \hat{u}_i \cdot \hat{n}) &= \frac{1}{2} \exp(-2\pi i f \hat{n} \cdot \mathbf{x}_{i1}) [\hat{u}_i \otimes \hat{u}_i T_{\text{MI}}(f, \hat{n} \cdot \hat{u}_i) \\ &\quad - \hat{v}_i \otimes \hat{v}_i T_{\text{MI}}(f, \hat{n} \cdot \hat{v}_i)], \\ D^{\beta_i}(f, \hat{u}_i \cdot \hat{n}) &= D^{\alpha}(f, \hat{u}_i \cdot \hat{n}) + \exp(-2\pi i f \hat{n} \cdot \mathbf{x}_{i3}) \\ &\quad \times [\hat{u}_i \otimes \hat{u}_i T_{\text{MI}}(f, \hat{n} \cdot \hat{u}_i) \\ &\quad - \hat{w}_i \otimes \hat{w}_i T_{\text{MI}}(f, \hat{n} \cdot \hat{w}_i)]. \end{aligned} \quad (21)$$

Following [33], we then combine Eq. (18) to form estimators sensitive to just intensity or circular polarization:

$$\begin{aligned} &\frac{1}{2} \delta_T(f - f') \mathcal{R}_I(f) I(f) \\ &\equiv \langle [s^{\alpha_1}(f) + s^{\beta_1}(f)] [s^{\alpha_2^*}(f') + s^{\beta_2^*}(f')] \rangle, \\ &\frac{1}{2} \delta_T(f - f') \mathcal{R}_V(f) V(f) \\ &\equiv \langle s^{\alpha_1}(f) s^{\beta_2^*}(f') - s^{\beta_1}(f) s^{\alpha_2^*}(f') \rangle. \end{aligned} \quad (22)$$

We will consider two experimental configurations of the two constellation, introduced in Ref. [33]: “LISA” with $L = 1 \times 10^9$ m, $D = 7$, $T = 10$ years, and “BBO” with $L = 5 \times 10^7$ m, $D = 2$, $T = 10$ years. These designs are optimized to achieve roughly equal sensitivity to I and V .

C. Interferometer signal-to-noise ratio

Under the assumption that the signals we are cross-correlating have independent noise properties and are Gaussian distributed, and that the noise spectrum dominates over the signal, then the signal-to-noise ratio in the interferometer is given by [33,64,65]

$$\left(\frac{S}{N}\right)_{I,V}^2 = 2T \int_0^\infty df \left(\frac{3H_0^2}{4\pi^2}\right)^2 \frac{|\mathcal{R}_{I,V}(f) \Omega_{\text{GW}}^{I,V}(f)|^2}{f^6 S_n^{I,V}(f)^2}, \quad (23)$$

where $S_n^{I,V}(f)$ is the power spectrum of the noise in the I, V signals, and $\Omega_{\text{GW}}^{I,V}$ is the fractional energy density of gravitational waves in intensity and circular polarization today, defined in Eq. (12). To find the background fractional energy density, we multiply the primordial spectrum by the appropriate transfer function [20,68,69]: $\Omega_{\text{GW}}^{I,V}(f) = \frac{\Omega_{R,0}}{24} (\mathcal{P}^L(f) \pm \mathcal{P}^R(f))$, where $\Omega_{R,0}$ is the fractional energy density in radiation today.

Up to this point, we have not discussed the noise because it vanishes in the cross-correlations we consider. However, it still contributes to the variance of the estimators in Eq. (22). There are three major sources of noise in measurements of a particular optical path through an interferometer: shot noise $S_{n,s}(f)$, accelerometer noise $S_{n,a}(f)$, and the dominant laser phase noise, $S_{n,\phi}(f)$. As pointed out in Sec. IV B, the major motivation for using equal-arm Michelson interferometers, as given in the first two lines of Eq. (18), is the cancellation of the laser phase noise. The shot and acceleration noises can be approximated by taking the fiducial LISA [37] and BBO [60] values and scaling them to an instrument with arm length L , observing at frequency f [64]. The final expressions for $S_n^{I,V}(f)$ are derived by Ref. [33]:

$$\begin{aligned} S_n^I(f) &= \frac{121}{4} \left[S_{n,s}(f) + 2S_{n,a}(f) \left(1 + \cos^2\left(\frac{f}{f_*}\right) \right) \right]^2, \\ S_n^V(f) &= \frac{96}{121} S_n^I(f), \end{aligned} \quad (24)$$

where the values for $S_{n,a}(f)$ and $S_{n,s}(f)$ for LISA and BBO are given in Ref. [33]. As is the case for the CMB, our galaxy contains sources of gravitational waves that may act as a confusion noise to a measurement of the GWB [70,71]. It is expected that compact binary systems in our galaxy will form a gravitational wave foreground with an amplitude in intensity of $\Omega_{\text{WD}} \sim 10^{-12}$ in the mHz regime. The shape of this spectrum is quite complicated because different periods of a binary system’s evolution dominate at different frequencies and have different frequency dependencies [70]. For the design of LISA we consider, we expect the impact of such a foreground to be small compared to the acceleration noise [72]. The BBO design we consider peaks at $\gtrsim 0.3$ Hz, which is expected to be relatively free of such sources of noise [73,74]. However, we are mainly interested in detecting chirality of the GWB, and this is more easily

distinguished from astrophysical foregrounds, and accordingly, previous studies have not considered polarized foregrounds [20,33,75]. Therefore, we do not consider a contribution to the noise from astrophysical foregrounds in intensity or in polarization, but it should be noted that we expect a small degradation in the achievable intensity sensitivity of the fiducial LISA design compared to our result, due to the confusion noise of astrophysical sources.

D. Interferometer results

In Fig. 10, we plot signal-to-noise contours for LISA assuming $k_p = 1 \times 10^{11} \text{ Mpc}^{-1}$, and in Fig. 11, we plot the corresponding contours for BBO assuming $k_p = 1 \times 10^{13} \text{ Mpc}^{-1}$. We see that both the LISA and BBO configurations may detect a polarized gravitational wave background with a signal-to-noise ratio greater than one in a regime unavailable to the CMB. In the case of LISA, the signal-to-noise ratio for $k_p = 1 \times 10^{13} \text{ Mpc}^{-1}$ is on the order of one. However, we see that a BBO-like design far exceeds the sensitivity of LISA, probing a much larger range of r for the large k_p values, inaccessible to CMB experiments. A single constellation design described in Sec. IV B 1 would achieve equivalent sensitivity in I to LISA and BBO but with no V sensitivity. Therefore, the fiducial LISA design would be sensitive to the inflationary model we consider here because a positive detection of I at these scales with no corresponding detection on CMB

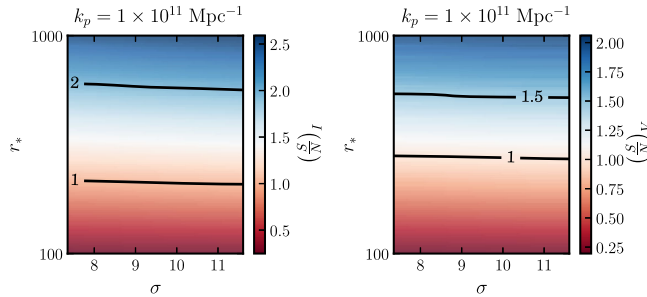


FIG. 10. Signal-to-noise contours obtained using Eq. (23) for a LISA-like experiment described in Sec. IV C. The primordial spectrum has $k_p = 1 \times 10^{11} \text{ Mpc}^{-1}$.

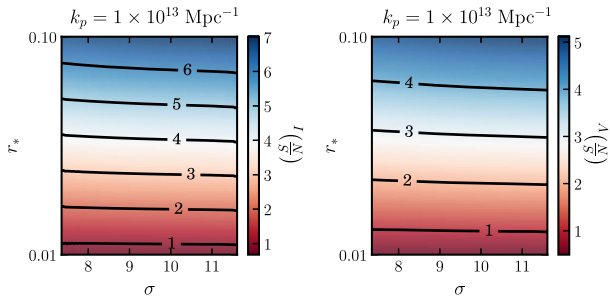


FIG. 11. Signal-to-noise contours obtained using Eq. (23) for a BBO-like experiment described in Sec. IV C. The primordial spectrum has $k_p = 1 \times 10^{13} \text{ Mpc}^{-1}$.

scales would require a strong scale dependence of the gravitational wave spectrum.

V. DISCUSSION

In this paper, we have considered for the first time the detectability of a new model for the production of gravitational waves proposed in Ref. [13]. Given the increasing effort to measure the B-mode spectrum of the CMB, this is an important step in establishing the origins of any detected primordial tensor perturbations. This model has a unique tensor spectrum characterized by its scale dependence and chirality, both of which we use in order to find observational markers that allow it to be distinguished from the conventional primordial gravitational waves produced by vacuum fluctuations. If a detection of primordial gravitational waves is made, and the markers we find to be detectable are absent, we may then rule out such a model. In Sec. III, we provided robust forecasts of the ability of the LiteBIRD satellite mission to detect the TB and EB correlations that result from the chiral tensor spectrum. We found that LiteBIRD would be able to detect the chirality for $r_* \gtrsim 0.03$, while $r_* < 0.07$ is required by current observations. The addition of Stage 4 observations has little effect as such a survey would be limited to $\ell > 30$, but the primordial chiral signal is contained almost entirely within $2 < \ell < 30$. Further, we found that for cosmic variance limited observations, the maximum achievable signal-to-noise ratio for $r_* < 0.07$ would be ~ 3 . From these studies, we conclude that the ability of CMB two-point statistics to determine the presence of a chiral GWB is fairly limited.

However, in this study, we have not fully leveraged the scale dependence of the axion- $SU(2)$ model. Single-field slow roll expects the tensor spectrum to have a tilt given by the self-consistency relation $n_T = -r/8$, and it would be possible to test departures from this using a combination of both CMB and interferometer constraints to provide a lever arm [76,77]. Such a study would be aided by future ground-based observations such as Simons Observatory or S4. In this study, we found that for a peak wavenumber in the range $k_p \sim 7 \times 10^{-5}$ to $5 \times 10^{-3} \text{ Mpc}^{-1}$ the primordial BB spectrum is detectable by LiteBIRD with $(S/N)_{BB} \gtrsim 1$ for $r_* \gtrsim 10^{-3}$. However, the projected sensitivity on n_T for LiteBIRD alone is ~ 0.04 , which is not sufficient to test deviations from the self-consistency relation, without external constraints.

Another characteristic of the axion- $SU(2)$ model of Ref. [13] is its intrinsic non-Gaussianity. Some studies have recently shown that higher order statistics of B-modes, such as the BBB bispectrum, may yield a $> 2\sigma$ significance for the axion- $U(1)$ model [12,19]. An analysis of the CMB non-Gaussianity for the axion- $SU(2)$ model is therefore in order [62].

In Sec. IV, we showed that interferometers may provide a complementary probe to the CMB at much smaller scales of $\sim 10^{12} \text{ Mpc}^{-1}$, even for the relatively flat spectra required by the attractor behavior of the background axion field coupled

to the $SU(2)$ gauge field. This takes advantage of the scale dependence of the axion- $SU(2)$ model, which allows the spectrum to have a large excursion at some scale k_p , e.g., as shown in Fig. 8, making the cosmological GWB of the axion- $SU(2)$ model a viable target for interferometers with current sensitivities. We went on to consider two designs of an advanced stage LISA-like mission proposed by Ref. [33] which are sensitive to both the intensity and circular polarization of the GWB. While interferometers are not, in general, sensitive to the same parameter space of the model as CMB probes, we found that for spectra with a very large values of k_p and σ , which would be undetectable on CMB scales, such experiments could make significant detections and therefore complement CMB constraints.

ACKNOWLEDGMENTS

B.T. would like to acknowledge the support of the University of Oxford-Kavli IPMU Fellowship and an STFC studentship. M. S. was supported in part by a Grant-in-Aid for JSPS Research under Grant No. 27-10917 and JSPS Grant-in-Aid for Research Activity Start-up Grant No. 17H07319. The work of T. F. is partially supported by the JSPS Overseas Research Fellowships, Grant No. 27-154. Numerical computations were in part carried out on Cray XC30 at Center for Computational Astrophysics, National Astronomical Observatory of Japan. We were supported in part by the World Premier International Research Center Initiative (WPI Initiative), MEXT, Japan. T. F. would like to thank Kavli IPMU for warm hospitality during his stay. This work was supported in part by JSPS KAKENHI Grant No. JP15H05896. M. H. and N. K. acknowledge support from MEXT KAKENHI Grant No. JP15H05891.

APPENDIX A: DERIVATION OF THE TEMPLATE FOR GW POWER SPECTRUM

In Ref. [13], it has been shown that the power spectrum of the sourced GW is given by

$$\mathcal{P}_h^{\text{L,Sourced}}(k) = \frac{\epsilon_B H_{\text{inf}}^2}{\pi^2 M_{\text{Pl}}^2} \mathcal{F}^2(m_Q), \quad (\text{A1})$$

where H_{inf} is the inflationary Hubble scale, $\epsilon_B \equiv g^2 Q^4 / (M_{\text{Pl}}^2 H_{\text{inf}}^2)$ roughly indicates the energy fraction of the $SU(2)$ gauge field. $\mathcal{F}(m_Q)$ is a monotonically increasing function for $3 \leq m_Q \leq 7$, which is well approximated by

$$\mathcal{F}(m_Q) \simeq \exp[2.4308m_Q - 0.0218m_Q^2 - 0.0064m_Q^3 - 0.86], \quad (3 \leq m_Q \leq 7), \quad (\text{A2})$$

where the value of a dynamical parameter $m_Q(t) \equiv gQ(t)/H_{\text{inf}}$ around the horizon crossing $k \sim aH_{\text{inf}}$ is substituted. Solving the background equations of motion for $\chi(t)$ and $Q(t)$ with the slow-roll approximation, one can show

$$m_Q(t) = m_* \sin^{1/3}[\chi(t)/f], \quad (\text{A3})$$

where $m_* \equiv (g^2 \mu^4 / 3\lambda H_{\text{inf}}^4)^{1/3}$ is the maximum value of $m_Q(t)$. From the definition of m_Q and ϵ_B , the value of ϵ_B at $m_Q = m_*$ is $\epsilon_{B*} \equiv H^2 m_*^4 / g^2 M_{\text{Pl}}^2$. Therefore, the tensor-to-scalar ratio r on the peak scale k_p of the sourced GW power spectrum is

$$r_* = \frac{\mathcal{P}_h^{\text{L,Sourced}}(k_p)}{\mathcal{P}_\zeta} = \frac{\epsilon_{B*} H_{\text{inf}}^2}{\pi^2 M_{\text{Pl}}^2 \mathcal{P}_\zeta} \mathcal{F}^2(m_*). \quad (\text{A4})$$

Next, we consider the width of the GW spectrum. Around the peak of $m_Q(t)$ at $t = t_*$, or $\chi(t = t_*) = \pi f/2$, $\chi(t)$ is expanded as

$$\chi(t) \simeq \frac{\pi}{2} f + \dot{\chi}_*(t - t_*) \simeq f \left[\frac{\pi}{2} + \frac{2\xi_*}{\lambda} H_{\text{inf}}(t - t_*) \right], \quad (\text{A5})$$

where $\dot{\chi}_* \equiv \dot{\chi}(t = t_*)$, $\xi_* \equiv \lambda \dot{\chi}_* / (2f H_{\text{inf}})$, and one can show $\xi_* \simeq m_* + m_*^{-1}$ in the slow-roll regime. Then we obtain the approximated equation for $m_Q(t)$, which is valid around the peak value,

$$m_Q(t) \simeq m_* \left[1 - \frac{1}{6} \left(\frac{H_{\text{inf}}(t - t_*)}{\Delta N} \right)^2 \right], \quad (t \sim t_*), \quad (\text{A6})$$

where we define $\Delta N \equiv \lambda/2\xi_*$. Substituting it into Eq. (A1) and using $H_{\text{inf}}(t - t_*) = \ln(k/k_p)$, we obtain the leading order result as

$$\mathcal{P}_h^{\text{L,Sourced}}(k) \simeq \frac{\epsilon_{B*} H_{\text{inf}}^2}{\pi^2 M_{\text{Pl}}^2} \mathcal{F}^2(m_*) \times \exp \left[-\mathcal{G}(m_*) \frac{\ln^2(k/k_p)}{\Delta N^2} \right], \quad (\text{A7})$$

with $\mathcal{G}(m_*) \approx 0.666 + 0.81m_* - 0.0145m_*^2 - 0.0064m_*^3$. Note that the contribution from $\epsilon_B(t) \propto m_Q^4(t)$ in the prefactor should not be missed. Comparing it with the template Eq. (2), one finds

$$\sigma^2 = \frac{\Delta N^2}{2\mathcal{G}(m_*)}. \quad (\text{A8})$$

The validity of the derived expression for $\mathcal{P}_h^{\text{L,Sourced}}(k)$ is checked by the comparison with the full numerical result. Once r_* , m_* , ϵ_{B*} and ΔN are fixed, all the model parameters g , λ , μ , and f are determined. Then we can numerically solve the background equation of $\chi(t)$ and $Q(t)$ as well as the equations for the perturbations $t_L(k, t)$ and $h_L(k, t)$ to obtain the power spectrum of the sourced GW. In Fig. 12, we compare the derived expression with the full numerical result. It should be noted that Eq. (A1) and our derivation rely on the slow-roll approximation. The approximation is less accurate for a small ΔN because ΔN characterizes the time scale of $\chi(t)$ rolling down its potential. In Fig. 12, one can find a small deviation in

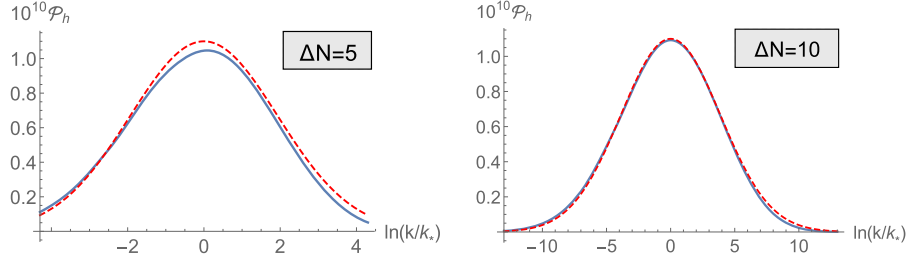


FIG. 12. Comparison between the full numerical result of $\mathcal{P}_h^{\text{Sourced}}(k)$ (blue solid line) and the template Eq. (2) with Eq. (A4) and $\sigma^2 = 0.15\Delta N^2$ (red dashed line). In the left (right) panel, $\Delta N = 5(10)$, $m_* = 4$, $\epsilon_{B*} \approx 9 \times 10^{-4}$, and the peak amplitude reaches the tensor-to-scalar ratio, $r_* = 0.05$. The Hubble parameter is set as $H_{\text{inf}} = 8 \times 10^{11}$ GeV, which corresponds to $r = 10^{-5}$ without the sourced GW. In the case of $\Delta N = 5$, the derived formula slightly underestimates the peak amplitude and the width, while the fit is excellent for $\Delta N \gtrsim 10$.

the case of $\Delta N = 5$, while the excellent agreement is seen for $\Delta N = 10$.

Finally, we discuss how long it takes χ to get to χ_* , given that the initial value of χ is negligibly small compared to $f\pi/2$. Assuming $\chi(t \approx 0) \ll f$ and using Eq. (A5), one finds

$$Ht_* \sim \frac{\pi}{2} \Delta N. \quad (\text{A9})$$

However, it is definitely underestimated because $\dot{\chi}(t \ll t_*)$ must be smaller than $\dot{\chi}(t = t_*)$, which is the maximum value. In fact, a full numerical calculation shows that the coefficient is somewhat larger,

$$Ht_* \approx 1.8\Delta N. \quad (\text{A10})$$

One may wonder if $\chi(t)$ can stay on the top of its potential hill for a longer time if its initial value is small enough. However, since χ is coupled to the $SU(2)$ gauge fields and the system quickly goes to the attractor behavior, the time scale of the motion of χ is almost solely determined by ΔN . It indicates that the peak scale k_p should be smaller than $k_i \exp[1.8\Delta N]$. Here, k_i is the wave number of the mode exiting the horizon at the initial time, and it is smaller or roughly equals the largest CMB scale. Therefore, we obtain the following constraint on ΔN ,

$$\Delta N \gtrsim \frac{1}{1.8} \ln\left(\frac{k_p}{k_{\text{CMB}}}\right). \quad (\text{A11})$$

APPENDIX B: CALCULATION OF THE COVARIANCE MATRIX, ξ

For a given beam, b_ℓ , and a white noise level, $w_{X_1 X_2}^{-1}$, the expected variance of the multipoles of an observed sky is given by

$$\langle (a_{\ell m}^{X_1})^* a_{\ell' m'}^{X_2} \rangle = (|b_\ell|^2 C_\ell^{X_1 X_2} + w_{X_1 X_2}^{-1}) \delta_{\ell \ell'} \delta_{m m'}. \quad (\text{B1})$$

An unbiased estimator of the angular power spectrum is then

$$\hat{C}_\ell^{X_1 X_2} = |b_\ell|^2 \left(\sum_{m=-\ell}^{\ell} \frac{(a_{\ell m}^{X_1})^* a_{\ell m}^{X_2}}{2\ell + 1} - w_{X_1 X_2}^{-1} \right). \quad (\text{B2})$$

By considering the expectation $\langle (\hat{C}_\ell^{X_1 X_2} - C_\ell^{X_1 X_2})(\hat{C}_\ell^{X_3 X_4} - C_\ell^{X_3 X_4}) \rangle$, it can then be shown that the covariance is given by [25]

$$\xi_{X_1 X_2 X_3 X_4} = \frac{1}{(2\ell + 1)f_{\text{sky}}} (\tilde{C}_\ell^{X_1 X_3} \tilde{C}_\ell^{X_2 X_4} + \tilde{C}_\ell^{X_1 X_4} \tilde{C}_\ell^{X_2 X_3}). \quad (\text{B3})$$

where $\tilde{C}_\ell^{X_1 X_2} = C_\ell^{X_1 X_2} + |b_\ell|^{-2} w_{X_1 X_2}^{-1}$.

APPENDIX C: CMB NOISE SPECTRUM

For a given set of experimental parameters such as channel frequencies, FWHM and sensitivity in polarization, and temperature per channel, we want to find the aggregate noise in the CMB spectra. We follow the treatment of Ref. [19], which itself closely follows Ref. [49].

There are multiple sources of noise in the final spectrum: instrumental noise in the CMB channels, residual foreground noise from incomplete cleaning, and additional systematic noise introduced from the templates used in cleaning the CMB channels.

The noise in the final CMB spectrum is

$$N_\ell^{BB} = \left[\sum_i \frac{1}{n_\ell(\nu_i) + [C_\ell^S(\nu_i) + C_\ell^D(\nu_i)]\sigma_{\text{RF}} + n_\ell^{\text{RF}}(\nu_i)} \right]^{-1}, \quad (\text{C1})$$

where the index i runs over channels used in CMB analysis, RF refers to residual foregrounds, $n_\ell(\nu)$ is the noise spectrum in the channels used for CMB analysis, $[C_\ell^S(\nu_i) + C_\ell^D(\nu_i)]\sigma_{\text{RF}}$ is the residual foreground level in dust and synchrotron rescaled to the frequencies used in CMB analysis, and $n_\ell^{\text{RF}}(\nu_i)$ is the instrumental uncertainty in the process of foreground removal.

The simplest of the above terms is the noise in the CMB channels:

$$n_\ell(\nu) = \sigma_P^2(\nu) \exp \left[\frac{\ell(\ell + 1) \left(\frac{\pi}{10800} \theta_{\text{FWHM}}(\nu) \right)^2}{8 \ln(2)} \right],$$

TABLE II. Spectral parameters used in noise model taken from Ref. [19].

Parameter	Value
A_S	$4.7 \times 10^{-5} \mu\text{K}^2$
α_S	-3
β_S	-2.6
$\nu_{S,0}$	30 GHz
$\ell_{S,0}$	350
A_D	$1 \mu\text{K}^2$
α_D	2.2
β_D	-2.5
$\nu_{D,0}$	94 GHz
$\ell_{D,0}$	10
T	18 K
p	0.15

where $\theta_{\text{FWHM}}(\nu)$ is the FWHM of the channel ν in arcminutes. The instrumental uncertainties in the process of foreground removal are given by Ref. [49]:

$$n_\ell^{\text{RF}} = \frac{4}{N_{\text{chan}}(N_{\text{chan}} - 1)} \left[\sum_j \frac{1}{n_\ell(\nu_j)} \right]^{-1} \times \left[\left(\frac{\nu}{\nu_{S,\text{ref}}} \right)^{2\alpha_S} + \left(\frac{\nu}{\nu_{D,\text{ref}}} \right)^{2\alpha_D} \right],$$

where N_{chan} is the number of channels used in foreground cleaning (in this case $N_{\text{chan}} = 10$), and $\nu_{S,\text{ref}}, \nu_{D,\text{ref}}$ are the highest and lowest frequency channel used in the removal (in this case $\nu_{S,\text{ref}} = 30$ GHz, $\nu_{D,\text{ref}} = 94$ GHz). The foreground spectra are

$$C_\ell^S(\nu) = A_S \left(\frac{\nu}{\nu_{S,0}} \right)^{2\alpha_S} \left(\frac{\ell}{\ell_{S,0}} \right)^{\beta_S},$$

$$C_\ell^D(\nu) = p^2 A_D \left(\frac{\nu}{\nu_{D,0}} \right)^{2\alpha_D} \left(\frac{\ell}{\ell_{D,0}} \right)^{\beta_D} \left[\frac{e^{\frac{h\nu_{D,0}}{k_B T}} - 1}{e^{\frac{h\nu}{k_B T}} - 1} \right].$$

These are converted into a Gaussian addition to the noise by the factor σ^{RF} such that a 2% residual level corresponds to $\sigma^{\text{RF}} = 4 \times 10^{-4}$.

The spectral parameters of the foregrounds are summarized in Table II. They are taken from Ref. [49] and are consistent with the 2015 Planck data.

APPENDIX D: FREQUENCY DEPENDENCE OF CMB SENSITIVITY

When we calculate the CMB angular power spectrum, we are decomposing the signal into multipoles

corresponding to a certain angular distance on the sky. Each multipole has contributions from all frequencies of the GWB, determined by an integral of transfer functions:

$$C_\ell^{YY'} = 4\pi \int \frac{dk}{k} [\mathcal{P}_h^L(k) - \mathcal{P}_h^R(k)] \Delta_{Y,\ell}^h(k) \Delta_{Y',\ell}^h(k).$$

This makes a direct link between multipole and frequency ambiguous. Since the transfer functions are sharply peaked at $k_\ell = \ell/\eta_0$ with η_0 denoting the comoving distance to the last scattering surface. We make the approximation,

$$\begin{aligned} C_\ell^{YY'}(k_\ell) &= \left[4\pi \int \frac{dk}{k} [\mathcal{P}_h^L(k, r_* = 1) - \mathcal{P}_h^R(k, r_* = 1)] \right. \\ &\quad \left. \times \Delta_{Y,\ell}^h(k) \Delta_{Y',\ell}^h(k) \right] (\mathcal{P}_h^L(k_\ell, r_*) - \mathcal{P}_h^R(k_\ell, r_*)) \\ &= C_\ell^{YY'}(r_* = 1) (\mathcal{P}_h^L(k_\ell, r_*) - \mathcal{P}_h^R(k_\ell, r_*)). \end{aligned} \quad (\text{D1})$$

To calculate the sensitivity to a circular background, we calculate the signal-to-noise ratio of the TB spectrum, ignoring the small contribution from EB for simplicity. The signal-to-noise ratio is therefore

$$(S/N)_{TB,\ell}^2 = (2\ell + 1) f_{\text{sky}} \frac{(C_\ell^{TB})^2}{\hat{C}_\ell^{TT} \hat{C}_\ell^{BB}},$$

where over-hat indicates the observed spectrum, including foreground residuals, instrument noise, and lensing. Our assumption that the transfer function is strongly peaked at k_ℓ now allows us to write this as a function of k_ℓ instead of just ℓ :

$$(S/N)_{TB}^2(k_\ell) = (2\ell + 1) f_{\text{sky}} \frac{(C_\ell^{TB}(k_\ell))^2}{\hat{C}_\ell^{TT} \hat{C}_\ell^{BB}}.$$

Note that we still calculate the observed spectrum fully. We then ask the question: what is the required $\mathcal{P}_h^L(k_\ell)$ (take $\mathcal{P}_h^R = 0$) to achieve a signal-to-noise ratio of one in the channel k_ℓ ? This will be the minimum GWB detectable with a signal-to-noise ratio of one. So,

$$\begin{aligned} &(\mathcal{P}_h^L(k_\ell, r_*) - \mathcal{P}_h^R(k_\ell, r_*))^{\text{min}} \\ &= \sqrt{\frac{\hat{C}_\ell^{TT} \hat{C}_\ell^{BB}}{(2\ell + 1) f_{\text{sky}}}} [C_\ell^{TB}(r_* = 1)]^{-1}. \end{aligned}$$

This quantity tells us about the tensor spectrum at recombination; however, in order to compare with interferometers which are sensitive to the current GWB, we have to evolve this forward in time. The tensor spectrum transfer function for CMB scales is [33,78]

$$\Omega_V^{\text{min}} h^2 = 1875 (\mathcal{P}_h^L(k_\ell) - \mathcal{P}_h^R(k_\ell))^{\text{min}} \left(\frac{3j_2(k_\ell \eta_0)}{k_\ell \eta_0} \frac{k_\ell}{k_*} \right)^2. \quad (\text{D2})$$

- [1] D. Baumann, M. G. Jackson, P. Adshead, A. Amblard, A. Ashoorioon, N. Bartolo, R. Bean, M. Beltrán, F. de Bernardis, S. Bird *et al.*, *AIP Conf. Proc.* **1114**, 10 (2009).
- [2] M. Kamionkowski and E. D. Kovetz, *Annu. Rev. Astron. Astrophys.* **54**, 227 (2016).
- [3] C. Guzzetti, M. N. Bartolo, M. Liguori, and S. Matarrese, *Riv. Nuovo Cimento* **39**, 399 (2016).
- [4] P. A. R. Ade, Y. Akiba, A. E. Anthony, K. Arnold, M. Atlas, D. Barron, D. Boettger, J. Borrill, S. Chapman, Y. Chinone *et al.* (The Polarbear Collaboration), *Astrophys. J.* **794**, 171 (2014).
- [5] R. Keisler, S. Hoover, N. Harrington, J. W. Henning, P. A. R. Ade, K. A. Aird, J. E. Austermann, J. A. Beall, A. N. Bender, B. A. Benson *et al.*, *Astrophys. J.* **807**, 151 (2015).
- [6] S. Naess, M. Hasselfield, J. McMahon, M. D. Niemack, G. E. Addison, P. A. R. Ade, R. Allison, M. Amiri, N. Battaglia, J. A. Beall *et al.*, *J. Cosmol. Astropart. Phys.* **10** (2014) 007.
- [7] P. A. R. Ade, Z. Ahmed, R. W. Aikin, K. D. Alexander, D. Barkats, S. J. Benton, C. A. Bischoff, J. J. Bock *et al.* (BICEP2 Collaboration, Keck Array Collaboration), *Phys. Rev. Lett.* **116**, 031302 (2016).
- [8] P. A. R. Ade, N. Aghanim, M. Arnaud, F. Arroja, M. Ashdown, J. Aumont, C. Baccigalupi, M. Ballardini, A. J. Banday *et al.* (Planck Collaboration) *Astron. Astrophys.* **594**, A20 (2016).
- [9] M. Hazumi *et al.* (LiteBIRD Collaboration), *Proc. SPIE Int. Soc. Opt. Eng.* **8442**, 844219 (2012).
- [10] P. de Bernardis, Core+ proposal, http://coresat.planck.fr/uploads/Mission/COReplus_proposal.pdf (2015), accessed 27-October-2016.
- [11] K. N. Abazajian, P. Adshead, Z. Ahmed, S. W. Allen, D. Alonso, K. S. Arnold, C. Baccigalupi, J. G. Bartlett, N. Battaglia, B. A. Benson *et al.*, [arXiv:1610.02743](https://arxiv.org/abs/1610.02743).
- [12] R. Namba, M. Peloso, M. Shiraishi, L. Sorbo, and C. Unal, *J. Cosmol. Astropart. Phys.* **01** (2016) 041.
- [13] E. Dimastrogiovanni, M. Fasiello, and T. Fujita, *J. Cosmol. Astropart. Phys.* **01** (2017) 019.
- [14] I. Obata, J. Soda (CLEO Collaboration), *Phys. Rev. D* **93**, 123502 (2016).
- [15] R. Z. Ferreira, J. Ganc, J. Noreña, and M. S. Sloth, *J. Cosmol. Astropart. Phys.* **04** (2016) 039.
- [16] C. Caprini and L. Sorbo, *J. Cosmol. Astropart. Phys.* **10** (2014) 056.
- [17] S. Mukohyama, R. Namba, M. Peloso, and G. Shiu, *J. Cosmol. Astropart. Phys.* **08** (2014) 036.
- [18] M. Peloso, L. Sorbo, and C. Unal, *J. Cosmol. Astropart. Phys.* **09** (2016) 001.
- [19] M. Shiraishi, C. Hikage, R. Namba, T. Namikawa, and M. Hazumi, *Phys. Rev. D* **94**, 043506 (2016).
- [20] J. Garcia-Bellido, M. Peloso, and C. Unal, *J. Cosmol. Astropart. Phys.* **12** (2016) 031.
- [21] A. Lue, L.-M. Wang, and M. Kamionkowski, *Phys. Rev. Lett.* **83**, 1506 (1999).
- [22] M. Kamionkowski, A. Kosowsky, and A. Stebbins, *Phys. Rev. D* **55**, 7368 (1997).
- [23] M. Zaldarriaga and U. Seljak, *Phys. Rev. D* **55**, 1830 (1997).
- [24] S. Saito, K. Ichiki, and A. Taruya, *J. Cosmol. Astropart. Phys.* **09** (2007) 002.
- [25] V. Gluscevic and M. Kamionkowski, *Phys. Rev. D* **81**, 123529 (2010).
- [26] M. Gerbino, A. Gruppuso, P. Natoli, M. Shiraishi, and A. Melchiorri, *J. Cosmol. Astropart. Phys.* **07** (2016) 044.
- [27] N. Aghanim, M. Ashdown, J. Aumont, C. Baccigalupi, M. Ballardini, A. J. Banday, R. B. Barreiro, N. Bartolo, S. Basak *et al.* (Planck Collaboration), *Astron. Astrophys.* **596**, A110 (2016).
- [28] A. Gruppuso, M. Gerbino, P. Natoli, L. Pagano, N. Mandolesi, A. Melchiorri, and D. Molinari, *J. Cosmol. Astropart. Phys.* **06** (2016) 001.
- [29] D. Molinari, A. Gruppuso, and P. Natoli, *Phys. Dark Universe* **14**, 65 (2016).
- [30] N. Seto, *Phys. Rev. D* **75**, 061302 (2007).
- [31] N. Seto and A. Taruya, *Phys. Rev. Lett.* **99**, 121101 (2007).
- [32] N. Seto and A. Taruya, *Phys. Rev. D* **77**, 103001 (2008).
- [33] T. L. Smith and R. Caldwell, *Phys. Rev. D* **95**, 044036 (2017).
- [34] T. Matsumura, Y. Akiba, J. Borrill, Y. Chinone, M. Dobbs, H. Fuke, A. Ghribi, M. Hasegawa, K. Hattori, M. Hattori *et al.*, *J. Low Temp. Phys.* **176**, 733 (2014).
- [35] T. Matsumura *et al.*, *J. Low Temp. Phys.* **184**, 824 (2016).
- [36] A. Ferté and J. Grain, *Phys. Rev. D* **89**, 103516 (2014).
- [37] P. Amaro-Seoane, S. Aoudia, S. Babak, P. Binétruy, E. Berti, A. Bohé, C. Caprini, M. Colpi, N. J. Cornish, K. Danzmann *et al.*, *GW Notes* **6**, 4 (2013).
- [38] N. Bartolo *et al.*, *J. Cosmol. Astropart. Phys.* **12** (2016) 026.
- [39] P. A. R. Ade, N. Aghanim, M. Arnaud, M. Ashdown, J. Aumont, C. Baccigalupi, A. J. Banday, R. B. Barreiro, J. G. Bartlett *et al.* (Planck Collaboration) *Astron. Astrophys.* **594**, A13 (2016).
- [40] P. Adshead, E. Martinec, and M. Wyman, *Phys. Rev. D* **88**, 021302 (2013).
- [41] E. Dimastrogiovanni and M. Peloso, *Phys. Rev. D* **87**, 103501 (2013).
- [42] T. Moroi and T. Takahashi, *Phys. Rev. D* **66**, 063501 (2002).
- [43] D. H. Lyth and D. Wands, *Phys. Lett. B* **524**, 5 (2002).
- [44] K. Enqvist and M. S. Sloth, *Nucl. Phys.* **B626**, 395 (2002).
- [45] J. R. Pritchard and M. Kamionkowski, *Ann. Phys. (Amsterdam)* **318**, 2 (2005).
- [46] D. Blas, J. Lesgourgues, and T. Tram, *J. Cosmol. Astropart. Phys.* **07** (2011) 034.
- [47] M. Zaldarriaga and U. Seljak, *Phys. Rev. D* **58**, 023003 (1998).
- [48] N. Katayama and E. Komatsu, *Astrophys. J.* **737**, 78 (2011).
- [49] Y. Oyama, K. Kohri, and M. Hazumi, *J. Cosmol. Astropart. Phys.* **02** (2016) 008.
- [50] D. O'Dea, A. Challinor, and B. R. Johnson, *Mon. Not. R. Astron. Soc.* **376**, 1767 (2007).
- [51] M. Shimon, B. Keating, N. Ponthieu, and E. Hivon, *Phys. Rev. D* **77**, 083003 (2008).
- [52] J. P. Kaufman, N. J. Miller, M. Shimon, D. Barkats, C. Bischoff, I. Buder, B. G. Keating, J. M. Kovac, P. A. R. Ade, R. Aikin *et al.*, *Phys. Rev. D* **89**, 062006 (2014).
- [53] R. Adam, P. A. R. Ade, N. Aghanim, M. Arnaud, M. Ashdown, J. Aumont, C. Baccigalupi, A. J. Banday, R. B. Barreiro *et al.* (Planck Collaboration), *Astron. Astrophys.* **594**, A8 (2016).

- [54] F. Nati, M. J. Devlin, M. Gerbino, B. R. Johnson, B. Keating, L. Pagano, and G. Teply, *J. Astron. Inst.* **06**, 1740008 (2017).
- [55] B. G. Keating, M. Shimon, and A. P. S. Yadav, *Ap. J.* **762**, L23 (2013).
- [56] M. H. Abitbol, J. C. Hill, and B. R. Johnson, *Mon. Not. R. Astron. Soc.* **457**, 1796 (2016).
- [57] R. Adam, P. A. R. Ade, N. Aghanim, M. Arnaud, J. Aumont, C. Baccigalupi, A. J. Banday, R. B. Barreiro, J. G. Bartlett *et al.* (Planck Collaboration) *Astron. Astrophys.* **586**, A133 (2016).
- [58] B. P. Abbott, R. Abbott, R. Adhikari, P. Ajith, B. Allen, G. Allen, R. S. Amin, S. B. Anderson, W. G. Anderson, M. A. Arain *et al.*, *Rep. Prog. Phys.* **72**, 076901 (2009).
- [59] T. Accadia, F. Acernese, M. Alshourbagy, P. Amico, F. Antonucci, S. Aoudia, N. Arnaud, C. Arnault, K. G. Arun, P. Astone *et al.*, *J. Inst.* **7**, P03012 (2012).
- [60] J. Crowder and N. J. Cornish, *Phys. Rev. D* **72**, 083005 (2005).
- [61] B. Allen, in *Relativistic Gravitation and Gravitational Radiation*, edited by J.-A. Marck and J.-P. Lasota (Cambridge University Press, Cambridge, England, 1997), p. 373.
- [62] A. Agrawal, T. Fujita, and E. Komatsu (to be published).
- [63] L. S. Finn, *Phys. Rev. D* **79**, 022002 (2009).
- [64] N. J. Cornish, *Phys. Rev. D* **65**, 022004 (2001).
- [65] J. D. Romano and N. J. Cornish, *Living Rev. Relativity* **20**, 2 (2017).
- [66] K. Somiya, *Classical Quantum Gravity* **29**, 124007 (2012).
- [67] N. J. Cornish and S. L. Larson, *Classical Quantum Gravity* **18**, 3473 (2001).
- [68] N. Barnaby, J. Moxon, R. Namba, M. Peloso, G. Shiu, and P. Zhou, *Phys. Rev. D* **86**, 103508 (2012).
- [69] L. A. Boyle and P. J. Steinhardt, *Phys. Rev. D* **77**, 063504 (2008).
- [70] A. J. Farmer and E. S. Phinney, *Mon. Not. R. Astron. Soc.* **346**, 1197 (2003).
- [71] B. S. Sathyaprakash and B. F. Schutz, *Living Rev. Relativity* **12**, 2 (2009).
- [72] A. Klein, E. Barausse, A. Sesana, A. Petiteau, E. Berti, S. Babak, J. Gair, S. Aoudia, I. Hinder, F. Ohme *et al.*, *Phys. Rev. D* **93**, 024003 (2016).
- [73] V. Ferrari, S. Matarrese, and R. Schneider, *Mon. Not. R. Astron. Soc.* **303**, 247 (1999).
- [74] C. Ungarelli and A. Vecchio, *Phys. Rev. D* **63**, 064030 (2001).
- [75] N. Seto, *Phys. Rev. D* **75**, 061302 (2007).
- [76] P. D. Meerburg, R. Hložek, B. Hadzhiyska, and J. Meyers, *Phys. Rev. D* **91**, 103505 (2015).
- [77] P. D. Lasky, C. M. F. Mingarelli, T. L. Smith, J. T. Giblin, E. Thrane, D. J. Reardon, R. Caldwell, M. Bailes, N. D. R. Bhat, S. Burke-Spolaor *et al.*, *Phys. Rev. X* **6**, 011035 (2016).
- [78] Y. Watanabe and E. Komatsu, *Phys. Rev. D* **73**, 123515 (2006).